Coastal Engineering

Combining field observations and fine-scale numerical modeling to demonstrate the effect of coral reef roughness on turbulence and its implications for reef restoration design

--Manuscript Draft--

Manuscript Number:	
Article Type:	Research Paper
Keywords:	Turbulence; Wave dissipation; Coral Reefs; Reef Restoration; OpenFOAM
Corresponding Author:	Benjamin Kenneth Norris, Ph.D US Geological Survey Santa Cruz, California UNITED STATES
First Author:	Benjamin Kenneth Norris, Ph.D
Order of Authors:	Benjamin Kenneth Norris, Ph.D
	Curt D. Storlazzi, PhD
	Andrew W. M. Pomeroy, PhD
	Kurt J. Rosenberger
	Joshua B. Logan
	Olivia M. Cheriton, PhD
Abstract:	Coral reefs are effective natural barriers that protect adjacent coastal communities from hazards such as erosion and storm-induced flooding. However, the degradation of coral reefs compromises their efficacy to protect against these hazards, making degraded reefs a target for restoration. There have been limited field and numerical modelling studies conducted to understand how an increase in coral reef roughness, as would occur due to restoration, can affect wave energy dissipation for a range of real-world wave and water level conditions. To address this knowledge gap, field measurements were collected over adjacent low-roughness and high-roughness reefs off Moloka'i, Hawai'i, USA, subjected to the same oceanographic forcing. Those field data to were then used to calibrate and validate OpenFOAM computational fluid dynamical models of the reef. These models were used to explore turbulent kinetic energy dissipation for a range of environmental conditions based on measurements from a suite of existing datasets and values from the literature. In general, wave dissipation scales with incident wave conditions, where greater dissipation occurred for shallow depths and shorter-period waves. This tendency for short-period waves to be more readily attenuated is supported by wave energy dissipation factors in the range of 0.1 – 5, which decline with increasing wave period. Near-bed turbulent kinetic energy dissipation also scales with incident wave conditions, where the greatest difference in dissipation between low and high relief cases occurs for short wave periods. Turbulence becomes less affected by bottom roughness as the wave period increases. The results presented here indicate that increasing the seabed roughness by 13% through coral reef restoration could enhance wave attenuation and turbulent energy dissipation by 0.5 – 1 order of magnitude, or by 45% per across-shore meter.

Highlights:

- Near-bed turbulence scales negatively with water depth and positively with incident waves.
- High relief corals generate greater turbulence above the bed under shorter wave periods.
- Increasing seabed roughness by 13% results in a 45% increase in energy dissipation per meter of coral restoration.

Combining field observations and fine-scale numerical modeling to demonstrate the effect of coral reef roughness on turbulence and its implications for reef restoration design

Benjamin K. Norris[1], Curt D. Storlazzi[1], Andrew W. M. Pomeroy[2], Kurt J. Rosenberger[1], Joshua B. Logan[1], and Olivia M. Cheriton[1]

[1]US Geological Survey, Pacific Coastal and Marine Science Center, 2885 Mission Street, Santa Cruz, CA 95060 USA

[2]University of Melbourne, School of BioSciences, Biosciences 4, The University of Melbourne, Royal Parade, Parkville Victoria 3052, AUS

Corresponding Author:
Benjamin K. Norris
US Geological Survey
Pacific Coastal and Marine Science Center
2885 Mission Street
Santa Cruz, CA 95060 USA
bknorris@usgs.gov

Review Disclaimer:

Highlights:

- Near-bed turbulence scales negatively with water depth and positively with incident waves.
- High relief corals generate greater turbulence above the bed under shorter wave periods.
- Increasing seabed roughness by 13% results in a 45% increase in energy dissipation per meter of coral restoration.

Abstract

Coral reefs are effective natural barriers that protect adjacent coastal communities from hazards such as erosion and storm-induced flooding. However, the degradation of coral reefs compromises their efficacy to protect against these hazards, making degraded reefs a target for restoration. There have been limited field and numerical modelling studies conducted to understand how an increase in coral reef roughness, as would occur due to restoration, can affect wave energy dissipation for a range of real-world wave and water level conditions. To address this knowledge gap, field measurements were collected over adjacent low-roughness and high-roughness reefs off Molokaʻi, Hawaiʻi, USA, subjected to the same oceanographic forcing. Those field data to were then used to calibrate and validate OpenFOAM computational fluid dynamical models of the reef. These models were used to explore turbulent kinetic energy dissipation for a range of environmental conditions based on measurements from a suite of existing datasets and values from the literature. In general,

wave dissipation scales with incident wave conditions, where greater dissipation occurred for shallow depths and shorter-period waves. This tendency for short-period waves to be more readily attenuated is supported by wave energy dissipation factors in the range of 0.1 – 5, which decline with increasing wave period. Near-bed turbulent kinetic energy dissipation also scales with incident wave conditions, where the greatest difference in dissipation between low and high relief cases occurs for short wave periods. Turbulence becomes less affected by bottom roughness as the wave period increases. The results presented here indicate that increasing the seabed roughness by 13% through coral reef restoration could enhance wave attenuation and turbulent energy dissipation by 0.5 – 1 order of magnitude, or by 45% per across-shore meter.

1 Introduction

Along tropical coastlines, coral reef platforms protect against hazards such as wave run-up, overtopping, flooding, and erosion by dissipating incident wave energy before it reaches the shore (e.g., Gourlay, 1994). Short-period wave motions are largely dissipated by wave breaking at the reef crest, whereas both long and short-period waves are dissipated by bottom friction across the reef flat (Pomeroy et al., 2012). Live corals present a complex, three-dimensional structure that produces a higher rate of wave energy dissipation over short distances compared to other coastal settings (Nelson, 1994). Hence, it is thought that coral reefs provide a higher capacity for coastal protection than most other marine ecosystems (Ferrario et al., 2014). From these and other ecosystem benefits, global coral reefs are valued in the hundreds of billions of dollars per annuum (Cesar et al., 2003; Spalding et al., 2017). However, despite their high value, coral reefs are currently in decline worldwide. An estimated 75% of the world's coral reefs are rated as threatened through a combination of climate change and anthropogenic stressors (Burke et al., 2011). As a result, there is growing concern regarding the capacity of stressed and degraded reefs to protect coastlines under present and future sea levels (Perry et al., 2015; Woodroffe and Webster, 2014). Nonetheless, recent work suggests that maintaining the structural complexity of coral reefs may be the best tool we have to mitigate flooding and erosion risks along tropical coastlines as sea levels rise (Quataert et al., 2015; Harris et al., 2018a).

Coral reef restoration is one method for reducing the flood risk to tropical coastal communities (e.g., Beck and Lange 2016). Large-scale coral restoration efforts started in the Indo-Pacific and Red Sea in the 1990s, and since have become widespread, with thousands of projects now completed worldwide (Young et al., 2012). However, a review by Fabian et al. (2013) of reef restoration projects found that the vast majority (90%) of restorations were designed specifically for coral recovery instead of coastal defense, and found little quantitative information on the coastal defense benefits of restoration projects because this aspect was rarely measured. Indeed, specific information regarding both ecological and engineering aspects of coral restoration for coastal defense, such as the restoration location, height, and appropriate bottom roughness, are still poorly understood (Ferrario et al., 2014).

To address these knowledge gaps, a recent study by Roelvink et al. (2021) determined that the greatest reduction in wave-driven flooding could be achieved with shallower coral restorations on the upper fore reef and reef flat due to enhanced wave breaking and frictional dissipation, respectively. However, this study only provides a large-scale perspective on coral restoration, as their hydrodynamic models were phase-averaged. Phase-averaged wave models simulate the stochastic properties of sea waves, utilizing empirical formulations to parameterize non-linear physics, and can only resolve slowly varying surf zone processes such as wave set-up and mean wave-driven currents. In contrast, phase-resolving models (i.e., those that resolve wave motions at time-scales shorter than individual waves) are designed to provide a more complete representation of non-linear physics, including wave breaking, shoaling, and turbulent energy dissipation. The drag induced by coral colonies reduces near-bed wave-orbital velocities, inducing turbulence that has important implications for biological and physical processes (e.g., feeding, larval dispersal, sediment transport, and wave dissipation). Although the topic of turbulence in coral reefs is generally well-understood (see a recent review by Davis et al. 2021), modelling at this scale for the purpose of coral reef restoration is not. Hence, a primary objective of this study is to investigate this interplay between bottom roughness, wave conditions, and energy dissipation for low- and high-roughness scenarios representing pre- and post-restoration conditions to understand the role of coral reef restoration in coastal protection.

Here, we study this relationship using a computational fluid dynamics **(CFD)** numerical model forced with a range of observed environmental conditions (water depths, wave heights, and wave periods) found across coral reef flats worldwide. The purpose of this study is to understand: (1) the transformation of wave heights across the reef; (2) the spatial distribution of turbulence near the seabed; (3) how changes in physical roughness affect wave and turbulent energy dissipation; and (4) how energy dissipation scales with incident conditions.

In the following sections, we first review how wave energy is dissipated in a coral reef environment. We then describe the field experiment conducted on the reef flat, the numerical model, model calibration and validation, and data analysis methodologies. The numerical modeling results are described in Section 4, and in Section **Error! Reference source not found.** we discuss under which incident conditions dissipation is maximized for a given bed roughness. We conclude in Section 6 with a discussion of the implications of this study to guide coral reef restoration design for coastal hazard risk reduction.

2 Background: Wave energy dissipation over coral reefs

Coastal flooding and erosion are the primary hazards created when wave energy is not sufficiently damped across coral reefs (Shepard et al., 2005; Storlazzi et al., 2011; Quataert et al. 2015). Flooding can be especially problematic for coastal regions adjacent to degraded reefs, where the loss of reef structural complexity results in a greater transference of wave energy to the shore (Quataert et al. 2015; Harris et al., 2018a). As waves approach the shore, they begin to interact with the reef when their wavelengths, λ, become comparable to the local water depth, h. As these waves shoal, they increase in height, H, relative to h until they become unstable and break. Hence, we define the wave breaking parameter γ as the ratio of H to h for any across-shore location. Common values for γ are 0.78 for monochromatic waves derived from solitary wave theory (Longuet-Higgins & Fenton 1974), 0.42 for root-mean-square (RMS) wave heights (H_{rms}) observed in the surf zone of beaches (e.g., Thornton & Guza, 1982), and 0.4 – 0.6 for coral reef flats (Harris et al., 2018b). Over coral reefs, the majority of sea-swell (SS; $T < 25$ s) wave energy is dissipated on the reef crest (Lowe et al., 2005). Incident waves with height ratios smaller than γ pass the reef crest onto the reef flat. The reef flat is often only a few meters deep causing waves to lose significant amounts of energy to dissipation by bottom friction.

For shore-normal waves, the one-dimensional wave energy equation is:

$$\frac{\partial F_j}{\partial x} = -\varepsilon_{b,j} - \varepsilon_{f,j} \qquad (1)$$

where F_j is the wave energy flux in the cross-shore direction x, $\varepsilon_{b,j}$ is wave dissipation due to wave breaking, $\varepsilon_{f,j}$ is dissipation due to bottom friction, and the subscript j indicates the *j-th* frequency component of a spectral wave distribution. F_j at any across-shore location is given by: $F_j = E_j C_{g,j}$, where E_j is the total (potential and kinetic) wave energy and $C_{g,j}$ is the group velocity per linear wave theory. The total wave energy flux F can be assessed through trapezoidal integration of Eq. (1) across all frequencies. In this paper, we consider waves propagating across bottom roughness at a relatively constant depth that is below the breaking threshold and so dissipation due to breaking can be neglected. Hence, Eq. (1) simplifies to:

$$\frac{\partial F_j}{\partial x} = -\varepsilon_{f,j} = -\frac{1}{4}\rho f_{e,j} u_{b,r} {u_{b,j}}^2 \tag{2}$$

where $f_{e,j}$ is the energy dissipation factor (discussed below), $u_{b,r}$ is a representative near-bottom wave orbital velocity, given by

$$u_{b,r} = \sqrt{\sum_{j=1}^{N} {u_{b,j}}^2} \tag{3}$$

and $u_{b,j}$ is the velocity corresponding to the *j-th* frequency component (Lowe et al., 2005). $u_{b,j}$ is estimated from the water surface elevation spectrum ($S_{\eta,j}$) using linear wave theory,

$$u_{b,j} = \frac{a_j \omega_j}{\sinh k_j h} \tag{4}$$

where k_j is the wavenumber, ω_j the wave radian frequency ($= 2\pi(1/T)$), and the wave amplitude is $a_j = \sqrt{2S_{\eta,j}\Delta f}$, with Δf the spectral bandwidth. The total wave energy dissipation, ε_f, between any two across-shore locations can be estimated by summing Eq. (2) over all frequencies.

The energy dissipation factor, f_e, and the related wave dissipation factor, f_w, have been experimentally linked to the cover of living corals and the structural complexity of coral reefs (e.g., Harris et al. 2018b). While f_e and f_w mathematically differ by a phase shift between bottom shear stress and wave orbital velocity, when both factors are compared, they exhibit large experimental scatter and hence are often assumed equal (Gon et al., 2020; Nielsen, 1992). As this study is principally concerned with energy dissipation, we will refer to the friction factor as f_e. Observational evidence suggests that for coral reefs, f_e is typically $O(0.1)$ but can be as large as $O(1)$ over reefs with high rugosity (Lentz et al., 2016; Lowe et al., 2005; Monismith et al., 2015). Following Lowe et al. (2005), f_e can be related to the ratio of the bed roughness, k_w, and the wave orbital excursion at the bed, A_b, as:

$$f_e = \exp\left[a_1\left(\frac{k_w}{A_b}\right)^{a_2} + a_3\right] \tag{5}$$

where $A_b = u_{b,r}T/2\pi$, and the coefficients a_1, a_2, and a_3 are empirically derived (e.g., Madsen et al., 1988; Nielsen, 1992; Swart, 1974). Here, we use the values provided by Nielsen (1992) for fully developed, rough turbulent flow: $a_1 = 5.5$, $a_2 = 0.2$, and $a_3 = -6.3$. Although it is possible to estimate the bottom roughness from hydraulics if both f_e and A_b are known, here we specify $k_w \approx 4\sigma_r$ following Lowe et al. (2005), where σ_r is the standard deviation of a measured bathymetric profile. Values of k_w, σ_r, and rugosity are all commonly used measures of physical roughness in coral reef experiments (e.g., Duvall et al. 2019). Per Eq. (5), f_e is directly proportional to k_w and is inversely proportional to A_b, so increases in k_w results in greater f_e at constant *T*, and increases in *T* results in lower f_e at constant k_w. Here, we will use Eq. (5) to contextualize the modeling results and demonstrate the relationship of wave energy dissipation for two types of bottom roughness by varying wave characteristics with numerical modeling.

3 Methods

3.1 Experimental design

An experiment was designed to obtain detailed bathymetric and hydrodynamic measurements on a fringing reef flat. A field study location was chosen to obtain measurements where the reef varied in roughness in shallow water (1 – 2 m). Structure-from-Motion (SfM) techniques were used to obtain bathymetric data that was sufficiently detailed to justify the application of a CFD numerical model. Field hydrodynamic measurements were also concurrently obtained. Using the field data, numerical models were calibrated and validated. These models were then used to test a series of scenarios representing wave conditions found across reef flats worldwide to investigate turbulent energy dissipation under these conditions.

3.2 Study area

The study area (21°5.25’ N, 157°9.25’ W) was located off Waiakane on the south shore of the island of Moloka‘i in the Hawai‘ian Archipelago (Figure 1a). The Moloka‘i fringing reef stretches 53 km along the island’s southern shore. The reef flat, a roughly horizontal surface with water depths ranging between 0.3 and 2.0 m, extends from the shoreline out to the reef crest that is approximately 700 m offshore. The reef crest, where most deep-water waves break, is relatively well-defined along most of southern Moloka‘i (Storlazzi et al., 2003). During summer the hydrodynamic environment of Moloka‘i is dominated by 5 – 10 m/s northeasterly trade winds that generate wind waves (*T* ~ 5 – 8 s) with offshore wave heights of *H* ~ 1 – 3 m as well as smaller 1 – 2 m, longer period (*T* ~ 14 – 25 s) south swells (Storlazzi et al., 2003). Trade winds are enhanced by sea-breezes that are typically generated in the afternoon, although the shallow reef crest controls the height of the waves that are not locally generated. Moloka‘i has a mixed, semi-diurnal tidal regime, with a mean daily tidal range of 0.6 m (Ogston et al., 2004).

3.3 Model of reef complexity

3.3.1 Coarse-scale Structure-from-Motion

A field experiment was undertaken in June 2018 to measure the morphology and hydrodynamics of the reef off Waiakane, Moloka‘i. A large-scale SfM survey of the reef covering approximately 300 m in the across-shore direction and 1000 m in the along-shore direction from the shoreline to the reef crest was conducted using an Unmanned Aerial System (UAS). The UAS’ flight path was designed in a ‘lawn mower’ pattern to allow the camera sensor to cover each section of the reef multiple times, which ensured accurate coverage with sufficient overlap in the along and across-shore directions. Prior to conducting the survey, ground control points were deployed along the beach and within the reef, then were surveyed in with real-time kinematic GPS to accurately georeference the UAS imagery. The aircraft was flown during the early morning to reduce glare hotspots produced by a high sun angle.

3.3.2 Fine-scale Structure-from-Motion

On the reef flat, two study sites were selected (~640 m from the shoreline and ~20 m apart in the alongshore direction) that represented “low” and “high” coral roughness (hereafter, “Low Relief” and “High Relief”; Figure 1d–e). To characterize the roughness at each site, an approximately 12-m diameter area was digitized to sub-centimeter scale using underwater SfM photogrammetry. To ensure sufficient coverage of each site, a method similar to Pizarro et al., (2017) was used: a swimmer photographs a circular area by spooling a line out and around from a central mooring point, allowing for consistent coverage of the survey site. For this experiment, a 1.2-m vertical pole for mooring with a 12-cm cylinder and a 6-m length of line was used. To provide scale for the images, 15 scale bars were distributed throughout the sample area; each ruler also had two targets (one at either end of the ruler at known distance), which were used as control points for the digital model. Three sweeps of the area were conducted for each site with the camera positioned at three different angles to fully resolve the complex, three-dimensional surface of the coral reef.

3.3.3 Integrated coarse and fine-scale bathymetry

Photogrammetric reconstruction of both the coarse-scale and fine-scale bathymetries was conducted using AgiSoft Photscan (Version 1.2.5). Full details of the procedures used in alignment and scaling of the images used to construct the three-dimensional models are described in Pomeroy et al. (2022) and Logan et al. (2021). In brief, unique points in each photo (key points) were matched across the set of photos by the software. Camera calibration parameters were used to threshold the key points to remove any that did not meet these requirements. After alignment, control points were added to improve the camera calibrations and to register the point clouds to a local geographic coordinate system. Dense topographic point clouds were generated, each consisting of tens of millions of individual points.

To create an integrated bathymetry for use in CFD mesh generation, both the coarse and fine-scale point clouds were combined using the freeware CloudCompare. The aim was to create a realistic rough surface to initialize the simulated hydrodynamics before reaching the fine-scale area within the model domain (Figure 1e–d). Since the fine-scale point clouds were referenced to a local coordinate system, they had to be manually rotated and positioned within the larger georeferenced UAS point cloud. After alignment, a circle with a 12 m diameter was cut out from the coarse-scale cloud, and the two clouds were integrated by converting them into a Standard Tessellation Language (STL) mesh with a resolution that ranged from 10s of centimeters to <1 centimeter. This process was repeated for the other fine-scale point cloud, resulting in two coarse-to-fine scale bathymetries for the Low and High Relief model domains. Hereafter, we use the term “patch” to describe the fine-scale area of the bathymetry within the numerical model domains.

Two-dimensional profiles were then extracted from the three-dimensional integrated surfaces to create bathymetric profiles for the numerical models. The fine-scale patch areas of the two-dimensional profiles correspond to a rugosity index of 1.08 for the Low Relief and 1.24 for the High Relief site. The rugosity index was calculated as the sum of the Euclidean distances of the bathymetry profile in each patch divided by the straight-line distance between the patch edges. Similarly, the standard deviation of the bathymetry σ_r is 0.09 for the Low Relief site and 0.14 for the High Relief site, corresponding to values of k_w = 0.36 and 0.58, respectively. The implications of these roughness scales, relative to the modeled conditions, are discussed in Section 4.

3.4 Field Measurements

The hydrodynamic climate of the reef flat was quantified with two RBR D|Wave tide and wave sensors that were deployed across the reef flat and spaced 55 m apart. Two instrumented frames were also deployed directly above the Low and High Relief sites on the reef flat (Figure 1c). Pressure measurements were recorded with the RBRs continuously at 2 Hz for 34 min every hour (n = 4,096 samples). With this arrangement, the offshore RBR1 measured incident conditions on the reef flat and the onshore RBR2 provided a local reference for conditions measured at the instrumented frames. Both frames were identical in design and instrumentation, which consisted of a downward-looking high-resolution 2-MHz Nortek Aquadopp acoustic Doppler current profiler (ADCP) that logged current velocities and pressure at 4 Hz for 34 min every hour (n = 8,193 samples). Measurements were collected with the pressure transducers and ADCPs for two days between 24 and 26 June 2018, which is the calibration period of the numerical models. The instrument data were post-processed for quality control following the routine outlined in Montgomery et al. (2008).

3.5 Field data analysis

The following parameters were calculated from the instrument data to provide the information necessary to calibrate and validate the numerical models (Section 3.6).

3.5.1 Wave height and period

For each RBR and ADCP burst, burst-averaged mean water levels (h) were calculated from the pressure data. Power spectra were computed from pressure time series using Welch's method (MATLAB, MathWorks Inc.), where smaller Hamming-windowed segments with 50% overlap were utilized to yield spectra with 32 equivalent degrees of freedom. Sea surface elevation spectra S_η were estimated from the power spectra using linear wave theory. The significant wave height H_s was computed as:

$$H_s = 4\sqrt{\int S_\eta \mathrm{d}f} \tag{6}$$

and the RMS wave height was computed as $H_{rms} = \sqrt{8\int_{f_1}^{f_2} S_\eta(f)\mathrm{d}f}$, by integrating between f_1 = 0.04 and f_2 = 0.30 Hz for the sea-swell (SS, T < 25 s) wave band, and between f_1 = 0.001 and f_2 = 0.040 Hz for the infragravity (IG, 25 s < T < 250 s) wave band. The peak wave period T_p was identified as the frequency band in the spectrum S_η with the greatest energy, and the mean T_m $(= m_0/m_1)$ and zero-crossing wave period T_z $\left(= \sqrt{m_0/m_2}\right)$ were estimated from the variance of water surface elevation (m_0), the first $\left(= \int f S_\eta(f)\,\mathrm{d}f\right)$, and the second moments $\left(= \int f^2 S_\eta(f)\,\mathrm{d}f\right)$ of the wave height spectrum (e.g., Wiberg & Sherwood, 2008).

3.5.2 Mean and oscillatory velocities

Time-averaged (mean) velocities were computed for every ADCP profile bin from (E_c) and north (N_c) velocities over each burst. Following Luhar et al., (2013), the mean velocity was assessed as the average of all individual samples (E_j and N_j) in the burst, e.g.,

$$E_c = \frac{1}{N}\sum_{j=1}^{N} E_j. \tag{7}$$

The mean velocities were then subtracted from the time record to calculate root-mean-squared oscillatory velocities, e.g.,

$$E_{w,rms} = \sqrt{\frac{1}{N}\sum_{j=1}^{N}\left(E_j - E_c\right)^2}\,. \tag{8}$$

The total mean horizontal velocity, $|U_c| = \sqrt{E_c^2 + N_c^2}$, and RMS oscillatory horizontal velocity. $|U_{w,rms}| = \sqrt{E_{w,rms}^2 + N_{w,rms}^2}$ were computed for each profile bin over each burst.

3.5.3 The dissipation rate of turbulence

Estimates of the turbulent kinetic energy (TKE) dissipation rate, ε, were computed from each burst of ADCP velocity measurements (n = 8,193 samples) using the structure function method of Wiles et al., (2006). In brief, this method uses differenced adjacent along-beam locations (“bins”) up to a number of lags (“bin distances”) along a profile of vertical velocities. This differencing technique has been shown to be effective at filtering out large-scale vertical variability, such as wave oscillations, that are not associated with inertial-subrange turbulence in shallow water environments (e.g., Norris et al., 2019). To calculate the TKE dissipation rate, time series of vertical velocity were detrended, then velocity differences along the profile were computed for lags ranging from 1 to 5 mm, producing a profile of TKE dissipation rate estimates up to 0.76 m (the ADCP profile length) in length. In Section 3.6.3, we compare observed profiles of the $U_{w,rms}$ and TKE dissipation rates to simulated values to validate the numerical models.

3.6 Numerical Model

3.6.1 Model Description

In this study, numerical simulations were conducted using OpenFOAM version-1912 (OpenFOAM, 2020). OpenFOAM is an open-source CFD package for solving continuous mechanics problems. It features several applications to pre- and post-process model test cases, including mesh generation tools (*blockMesh*, *snappyHexMesh*), setting field values, mesh decomposition, and mesh sampling during and after runtime. Within OpenFOAM, the Volume of Fluid (VoF) solver *interFoam* was used to solve the three-dimensional Navier-Stokes equations using a RANS approach, comprising the continuity and momentum equations:

$$\nabla U = 0 \tag{9}$$

$$\frac{\partial \rho \boldsymbol{U}}{\partial t} + \nabla\cdot(\rho\boldsymbol{U}\boldsymbol{U}) - \nabla\cdot\left(\mu_{eff}\nabla\boldsymbol{U}\right) = -\nabla p^* - \boldsymbol{g}\cdot\boldsymbol{X}\nabla\rho + \nabla\boldsymbol{U}\cdot\nabla\mu_{eff} + \sigma_T\kappa_c\nabla\alpha \tag{10}$$

where the bold letters indicate a vector field, $\boldsymbol{g}$ the acceleration of gravity, $\boldsymbol{X}$ the position vector, $\boldsymbol{U}$ the velocity field in Cartesian coordinates, ρ is the fluid density, p^* is a modified pressure adopted by removing hydrostatic pressure– (e.g., $\rho\boldsymbol{g}\cdot\boldsymbol{X}$) from the total pressure, σ_T the surface tension coefficient (= 0.07 kg/s^2), κ_c the interface curvature, α the fluid phase fraction, and μ_{eff} the effective dynamic viscosity. The μ_{eff} was calculated as $\mu_{eff} = \mu_t + \mu$, with μ_t the dynamic turbulence viscosity estimated with the turbulence model ($k - \varepsilon$; described below).

The volume of fluid method (Hirt & Nichols, 1981) represents the phase fraction α within each cell of the model domain such that α = 0 corresponds to the air phase, α = 1 the water phase, and α = 0.5 the free surface. In the model, the phase fraction is governed by the advection equation under the given velocity field $\boldsymbol{U}$:

$$\frac{\partial \alpha}{\partial t} + \nabla \cdot \boldsymbol{U}\alpha + \nabla \cdot \left(\boldsymbol{U}_r \alpha(1-\alpha)\right) = 0 \tag{11}$$

where $\boldsymbol{U}_r$ is the compression velocity, a term that is only active in the free surface region due to the term $\alpha(1-\alpha)$. The advection and sharpness of the free surface is controlled by the MULES ("Multi-Dimensional Limiter for Explicit Solution") algorithm to improve interface accuracy. Our models used the PIMPLE algorithm to iteratively solve the momentum and continuity equations. The adaptive time step was controlled by a maximum Courant condition *maxCo* ($C_o = \Delta t|U|/\Delta x$, where Δt is the time step, $|U|$ is the velocity magnitude through a cell, and Δx is the cell size in the direction of the velocity), and a maximum interface Courant number *maxAlphaCo*. In this study, all simulations were carried out by setting *maxCo* and *maxAlphaCo* to 0.2.

To simulate waves, a special set of boundary conditions is required for *interFoam* to create the appropriate time-dependent velocity field and surface elevation at the model inlet, and a non-reflective boundary at the outlet. Although other alternatives exist, we used the IHFOAM toolbox (Higuera et al., 2013) to generate waves in the model domain as it has been shown to be robust and computationally efficient (e.g., Vyzikas et al., 2018). IHFOAM can simulate realistic waves according to several different wave theories, including Stokes I, II, and V, cnoidal, and irregular (random) waves.

Turbulence was modeled using the $k-\varepsilon$ closure scheme. Two-equation turbulence models are known to cause over-predicted turbulence levels beneath waves in numerical wave flumes, leading to un-physical wave decay over long propagation distances (Devolder et al., 2017). Hence, the turbulence model was stabilized using the method developed by Larsen & Fuhrman (2018), using their default parameter values for the $k-\varepsilon$ closure scheme. Other turbulence closure schemes ($k-\omega$, $k-\omega SST$) were initially considered, but early sensitivity testing revealed an insignificant effect of the choice of closure scheme on the model output. As the TKE dissipation rate (ε) was one of the desired model outputs, the $k-\varepsilon$ scheme provided the most direct method for extracting this value from the simulations.

3.6.2 Model Configuration

Two model domains were developed using the integrated 3D bathymetric surfaces for the Low and High Relief sites. Each domain was defined in a longshore uniform, two-dimensional vertical (2DV) coordinate system (x, z), with x pointing shoreward, z pointing upward, and the origin at the still water level (Figure 1d–e). The initial mesh was 55 m long and 6.5 m high, with a uniform resolution of 0.25 m. Model domains intersected the middle of each fine-scale patch to include the point where the ADCPs were deployed. The water depth in the calibration models (Section 3.5.1) was set to 1.2 m to match the average field conditions at each site during the calibration phase. The bathymetry was 'snapped' to the model domain with *snappyHexMesh* using three levels of grid refinement (i.e., $\Delta x = 0.125$, 0.06, and 0.03 m) in the free surface region and the fine-scale patch areas (Figure S1).

The bed and atmosphere were treated with *zeroGradient* and *inletOutlet* boundary conditions, respectively, with walls set as *empty* (non-computational) boundaries. At the model inlet, outlet, and along the bed, the *fixedFluxPressure* boundary condition was applied to the pressure (hydrostatic pressure) field to adjust the pressure gradient so that the boundary flux matched the velocity boundary condition. Turbulence parameters (k, ε) used respective wall functions to model boundary layer effects near the bathymetry. Time-averaged values of the dimensionless wall distance z^+ ranged from 35 to 120 for the calibration models, where

30 < z^+ < 300 defines the log-law layer where wall functions are applicable. To minimize numerical dissipation in the models, a second-order unbounded numerical scheme was used for gradients, second-order bounded central differencing schemes for divergence, and an unbounded second-order limited scheme was used for the Laplacian surface normal gradients. Wave boundary conditions were handled by IHFOAM.

For the calibration cases, an irregular wave field was supplied to the models by discretizing the surface pressure spectrum from RBR1 into 47 wave components (i), each defined by a wave height (H_i) wave period (T_i), wave phase (ψ_i), and wave direction (β_i) between 0.04 and 0.3 Hz. We specifically chose to focus on sea-swell, rather than infragravity waves, for the numerical models due to the necessity of running several computationally expensive models over multiple wave cycles to establish quasi-steady conditions for sampling. Since the infragravity waves were much smaller than sea-swell waves during the calibration period of the models (Figure 2), this was a reasonable assumption. For simplicity, it was assumed based on the field measurements that all waves propagated along the x-axis of the model domains and so $\beta = 0$.

The simulations were run for about 15 wave cycles (512 s), which included a 64 s spin-up period (*rampTime*) to allow flow conditions to reach a fully developed state. The calibration models were executed on 12 distributed parallel processors on an 18-core Intel i9-10980XE CPU at 3.75 GHz with 64 GB of RAM over a period of approximately 8 h. Sampling was conducted during model runtime for the area encompassing the fine-scale patch of the model domains. Data analysis was conducted on the last 10 wave cycles of each run (i.e., after a quasi-steady state was established).

3.6.3 Model Validation

To validate the model, the numerical results were compared to the observed sea-surface spectra, the mean RMS oscillatory horizontal ($U_{w,rms}$) and vertical ($W_{w,rms}$) velocities, and ε measured at the same location by the ADCP during the field experiment (i.e., Figure 1d–e). The predictive skill of the model was determined by calculating the bias and scatter index (SCI) as proposed by Van der Westhuysen (2010) for wave models. In general, there was excellent agreement between the measured and modeled free surface in both domains (not shown; *RMSE* < 3%), as well as in the near-bed velocity and turbulence profiles (Figure 3; R^2 = 0.73 – 0.97).

To evaluate grid-scale independence of the numerical solution, a series of five models were developed, each varying the level of grid cell refinement from very coarse at Level 1 (minimum cell length $\Delta x = 0.15$ m) to very fine at Level 5 ($\Delta x = 0.01$ m) (Appendix A). This test revealed that velocity profiles converged at Level 3 and above, indicating the calibration models (which used Level 3 grid cell refinement) produced grid-cell-size-independent solutions (Figure A1). The grid refinement models were also assessed according to the total wave energy dissipation estimated from the instrument data during the calibration period, which determined that Level 4 refinement ($\Delta x = 0.015$ m) was best suited for the remainder of the model simulations (Appendix A).

After validation, a series of models were developed for both the Low and High Relief domains to estimate ε across the fine-scale patches under a range of conditions found in natural coral reef ecosystems. A literature review of 12 studies and former USGS field deployments (Table 1) was used to generate combinations of observed hydrodynamic conditions. Four water depths (h = 1, 2, 3, 4 m), five significant wave heights (H_s = 0.4, 0.8, 1.2, 1.6, 2 m), and five peak wave periods (T_p = 4, 8, 12, 16, 20 s) were selected to span the range of recorded conditions. Combinations of conditions that were physically unreasonable, i.e., those with excessive wave steepness (H_s/λ > 0.142) or those above the theoretical breaking limit (γ > 0.78) were eliminated, resulting in 70 cases per domain and thus 140 total cases. A summary of the model scenarios is provided in Table 2.

The scenario models were set up by varying the vertical position of the bathymetry to create domains with four different water depths. Different wave generation theories according to Le Méhauté (1967) for each combination of h, H_s, and T_p were applied at the inlet boundary to drive wave flows through the model domains. Each model was executed for a total time of 2*T_p + 10*T_p to generate two wave cycles during spin-up followed by 10 wave cycles that were used for subsequent data analysis. To improve runtime efficiency, three models were run simultaneously on six distributed parallel processors on the same 18-core CPU. Execution times varied by model scenario and ranged from approximately 12 to 160 hours.

3.6.4 Model data analysis

Data derived from the numerical simulations were processed similarly to the field data. Estimates of H_s were calculated with Eq. (6) by discretizing time series of water surface elevation at select locations within each model domain: one location was next to the model inlet to provide incident conditions (H_{s0}), and an additional 12 locations (every meter) within the fine-scale patch area of the model domains (Figure 1d–e). These latter 12 estimates were then spatially averaged to determine the spatial mean significant wave height $\langle H_s \rangle$ across the Low or High Relief patches. Velocity and turbulence results from each fine-scale patch area were binned into 100 points along the x-z plane. As conditions varied across model scenarios, we chose to normalize the modeled TKE dissipation rates using the magnitude of U_w, which estimates total fluid motion from waves, and was computed from the RMS velocities (Eq. 7 – 8) assuming perfect sinusoids, i.e., $U_w = \sqrt{2}U_{w,rms}$. Estimates of $\partial F/\partial x$ were assessed from the model inlet across the fine-scale patch (the change in wave energy flux; Eq. 2) to compare with the spatial change in H_s wave height described above. The f_e were computed from the total mean ε_f and $u_{b,r}$ (Eq. 2 – 4). In Section 4, we compare f_e against the ratio of A_b to k_w (Eq. 5) to establish a relationship between the forcing conditions, bottom roughness, and energy dissipation.

4 Results

4.1 An overview of wave-driven currents and vortices

The results from an example Low and High Relief model with identical forcing conditions (h = 2 m, H_s = 0.8 m, T_p = 16 s) presented in Figure 4 demonstrate the modification of the wave flow field by the rough bathymetry. Maximum velocities occur beneath the wave crests as they propagate across the model domains. Unlike the Low Relief case in Figure 4a, the wave crest in the High Relief case appears to shoal as it propagates through the model, which could be indicative of greater energy dissipation over rougher bathymetry. As the wave crests propagate, small zones of enhanced mean flow form above the bed (denoted in dashed boxes in Figure 4) which are followed by circular eddies that form after the wave crest has passed. These eddies are the manifestation of turbulent energy dissipation.

4.2 Wave attenuation and dissipation

As waves propagate across the model domain, wave height attenuation and energy dissipation ($\partial F/\partial x$) occur as near-bed turbulence strips energy from the flow field. For the Low Relief cases, wave height attenuation is greatest (smaller ratios of $\langle H_s \rangle / H_{s0}$) under conditions with lower h and shorter T_p (Figure 5). The High Relief cases present a similar pattern, except with greater attenuation than the Low Relief cases at the same h and T_p. For the models with greater depth (h = 3 – 4 m), wave height attenuation becomes relatively constant between T_p = 12 – 20 s.

The patterns of $\partial F/\partial x$ mirror those observed in the wave height and energy attenuation, with the greatest dissipation occurring under short T_p for either the Low or High Relief cases (Figure 6). The greatest difference between the Low and High Relief cases occurs under shallower (h = 1 – 2 m) conditions but become similar for the deeper (h = 3 – 4 m) conditions. The tendency for wave dissipation to increase overall with increasing h may have to do with the greater transmittance of wave energy across the models as the water depth increases.

It is important to note that, as the wavelength, λ, differs between the model scenarios presented here (for example, a wave of H_s = 0.4 m at T_p = 4 s in h = 2 m of water has λ ~ 13 m, whereas a similar wave of H_s = 0.4 m at T_p = 20 s in h = 2 m of water has λ ~ 76 m), the averaging width of the fine-scale patch area (12 m) may not capture all changes in relative wave height. A simple explanation for why $\langle H_s\rangle/H_{s0}$ approaches 1 for both the Low and High Relief cases could therefore be related to spatial averaging over increasingly longer λ. However, there is also a physical explanation for this pattern, which is discussed in Section 4.5. In the next section, we investigate the magnitudes and vertical scale of near-bed turbulence for a subset of the models.

4.3 Depth profiles of model results

Results from 20 model runs (h = 1 – 4 m, H_s = 0.4 m, and T_p = 4 – 20 s) of space-and-time mean turbulence and wave velocities are presented in Figure 7 and 8 for the Low and High Relief sites, respectively. Comparing the figures, it is evident that the High Relief models (Figure 8a–d) produce greater overall turbulence (with magnitudes exceeding 10^{-2} m^2/s^3) than the Low Relief models (magnitudes of 10^{-3} m^2/s^3; Figure 7a–d). In both cases, this peak turbulence occurs in shallower depths and weakens with increasing h. For the Low Relief models, the depth profiles of the mean wave velocities ($\langle\overline{U_w}\rangle$; Figure 7e–h) resemble the logarithmic profile expected for smooth bed surfaces. In contrast, the High Relief cases demonstrate a more substantial modification of the mean wave velocities, with the formation of two wave boundary layers; the boundary layer is larger at the top of the roughness, and smaller closer to the bed. This pattern is most evident in Figure 8f for the h = 2 m, T_p = 20 s model. Considering the profiles of mean normalized *TKE* dissipation $\langle\bar{\varepsilon}\rangle/\langle\overline{U_w}^3\rangle$ (Figures 7i–l and 8i–l), normalized turbulence is greatest in the h = 2 m cases and reaches a maximum value under T_p = 12 s but does not change substantially under longer wave periods. Although normalized turbulence is also high in the h = 1 m models, these cases do not follow the same consistent pattern above the roughness layer as the deeper water cases. This irregularity may be because the long period waves (T_p = 12 – 20 s) are so damped by the shallow water that flow velocities and hence turbulence are diminished relative to the other wave periods.

4.4 Total mean turbulence for the low versus high relief reefs

The normalized turbulence data averaged into a single mean value as a function of γ for each model scenario is presented in Figure 9. Consistent with Figures 7 and 8, greater energy dissipation occurs for either Low or High Relief cases under greater γ (recalling $\gamma = H_s/h$) at constant wave period. The maximum energy dissipation occurs under the longest wave periods. For Low Relief cases, there is a greater spread in dissipation between shorter and longer periods, and normalized dissipation values for the T_p = 16 – 20 s approach that of the High Relief cases. For High Relief cases, there is less spread between shorter and longer periods, with shorter periods exhibiting greater dissipation compared to Low Relief cases. This pattern is more evident in Figure 10, which indicates there is nearly one order of magnitude difference between the Low and High Relief cases for shorter wave periods (T_p =

4 – 8 s; Welch's *t*-test, t = 6.6 – 7.5, df = 13 – 14, p < 0.001). However, this difference becomes less significant with increasing wave period (T_p = 12 – 16 s; t = 2.5 – 2.8, df = 14 – 21, p < 0.01), until at higher wave periods the difference is no longer significant (T_p = 20 s; t = 1.5, df = 12, p > 0.05), and several Low Relief cases equal or exceed the corresponding High Relief cases. In summary, energy dissipation at the bed is greatest for shorter period waves over rough surfaces, but this difference diminishes as the wave period increases until dissipation is nearly equivalent, regardless of the bottom roughness.

To determine which of the forcing conditions (h, H_s, or T_p) had the greatest effect on ε, data from all Low and High Relief cases were regressed using a stepwise multiple linear regression model. For the Low Relief models, all three variables contribute to dissipation, collectively explaining 46% of the variance in ε ($RMSE$ = 0.75; F = 16.4; p < 0.01). H_s the most significant predictor in the response in turbulence ($p \ll 0.01$), and h the least (p = 0.03). For the High Relief models, only the significant wave height (H_s) and wave period (T_p) can explain 53% of the variance in ε ($RMSE$ = 0.70; F = 33.4; p < 0.01), again with H_s as the most important predictor in the response in turbulence. In summary, ε decreased with increasing water depth and increased with increasing significant wave height and period. The exclusion of h in the High Relief regression model could indicate that turbulence is more strongly dependent on the other two forcing conditions. However, when the data are segregated by wave period, the water depth clearly still influences turbulence (Figures 7 and 8).

4.5 Wave energy dissipation factors

The tendency for shorter-period waves to be more readily dissipated over greater bottom roughness (parameterized by k_w) can be explained through the energy dissipation factor, f_e. For Low and High Relief cases, there is a trend of decreasing f_e with increasing A_b at constant k_w (Figure 11). The High Relief cases have a greater range of f_e than the Low Relief cases, from as large as ~5 under short period (T_p = 4 s) waves, to as small as ~0.005 under long period (T_p = 20 s) waves. To help visualize trends, empirical power law relationships were fit to each dataset. Power fits explain 51% of the observed variance in the Low Relief cases, and 80% of the variance in the High Relief cases. Nielsen's (1992) empirical relationship (Eq. 5) with $k_w \approx 4\sigma_r = 0.36$ and 0.58 for Low and High Relief cases, respectively, is computed for comparison (Figure 11). Despite some scatter, the Low Relief data generally follow the slope of the Nielsen relationship, but the High Relief data do not. The High Relief cases have a greater slope than the Low Relief cases, implying that the conversion of wave momentum into turbulence occurs at a faster rate over rougher surfaces. The discrepancy between the High Relief cases and the Nielsen relationship might be explained by the fact that Nielsen's relationship was calibrated based on laboratory experiments spanning a higher range of A_b/k_w than those considered here.

5 Discussion

This study presents a first attempt to quantify how increased bottom roughness, which could occur as a consequence of a coral reef restoration project, modifies local wave and turbulent energy dissipation. The bathymetric variability of our High Relief site (σ_r = 0.14) is similar to the reef described in Lentz et al. (2016) (σ_r = 0.13 in their study), whereas our Low Relief site (σ_r = 0.09) is similar to the rough-reef case (σ_r = 0.07) described in Jaramillo & Pawlak (2011). Similarly, the calculated values of energy dissipation factors are well in the range of observed values from hydrodynamically smooth, low relief reefs (e.g., f_e = 0.09; Cheriton et al. 2016) to hydrodynamically rough, high relief reefs (e.g., f_e = 5; Lentz et al. 2016), with the largest energy dissipation values associated with the smallest wave periods. Lowe et al. (2005) determined that when the wave-orbital excursion length is equivalent to the physical roughness length, wave motions inside the roughness are greatest and therefore wave energy dissipation is maximized. In our model results, this situation occurs in the shorter wave period cases (Figures 5, 6 and 11; $T_p = 4 – 8$ s). As the wave-orbital excursion length increases relative to the roughness, wave motions inside the roughness decline, resulting in lower wave energy dissipation (Figures 5, 6 and 11; $T_p = 16 – 20$ s).

The trend of decreasing wave height attenuation and energy dissipation at greater wave periods (Figures 5 and 6) appears to contrast the patterns in Figures 7 and 8, where greater bulk mean wave velocities correspond with longer wave periods and greater bulk mean TKE dissipation rates. To reiterate, these latter bulk mean values were assessed across the fine-scale patch area in each model domain, whereas the wave energy dissipation was assessed from the model inlet across the fine-scale patch. Re-evaluating the wave energy dissipation across only the patch indicates that the bulk mean TKE dissipation accounts for up to 41% of the total wave energy dissipation. Based on studies of frictional dissipation over coral reefs (Huang et al., 2012; Sous et al., 2020), it is expected that the dissipation of wave energy assessed via linear wave theory should be roughly equivalent to the TKE dissipation for friction-dominated environments. This discrepancy in the present work indicates our model may not precisely represent energy losses near the bed and may underestimate TKE dissipation by several percent. Regardless, the tendency for short-period waves to be more readily attenuated could explain why the TKE dissipation rates tended to be greater for the High Relief cases at constant γ compared to the Low Relief cases (Figures 9 and 10). The threshold wave period where normalized TKE dissipation rates are roughly equivalent between Low and High Relief cases (approximately $T_p = 16$ s for the conditions presented here), could represent the point at which wave orbital excursions are much longer than the scale of bottom roughness (e.g., Lowe et al. 2005), and instead turbulence becomes more strongly controlled by the bulk mean wave velocity.

The results presented here, however, are not without limitations. First, the simplification of real surface roughness, by translating this detail in SfM, and then by downsampling the SfM in the CFD models, likely underestimates fine-scale hydrodynamic effects at the scale of individual coral polyps (~1 cm). Second, the CFD model assumes the bed is impermeable, and although roughness is modeled with a function to describe turbulent boundary layers, this again is a simplification of the hydrodynamics of flows through porous media like coral heads. If porosity is considered, wave-induced currents (and hence, turbulence) are found to decrease with increasing bed porosity (Wen et al., 2020). Third, 2DV models neglect any three-dimensional effects such as flow around coral heads. Flows become more complex when considered in 3D but the general physical principals should remain similar to 2DV cases. Still, studies of the interactions of waves and complex three-dimensional reef bathymetry with phase-resolving numerical models are uncommon owing to the large computational effort required for such simulations. Despite these limitations, the results presented in the present paper reproduce similar patterns of wave and turbulent energy dissipation as found in natural coral reefs.

To summarize these findings in the context of coral restoration for coastal hazard risk reduction, the greatest effect could be achieved by increasing bed roughness (outplanting corals) in relatively shallow depths (1 – 2 m) in environments dominated by waves with shorter periods (4 – 12 s). Our results suggest that increasing the bed roughness by 13% from a rugosity of 1.08 (the Low Relief case) to 1.24 (the High Relief case) could enhance the rate of wave attenuation and increase turbulent energy dissipation at the bed by 0.5 to 1.0 order of magnitude (Figure 10). This change in bottom roughness would translate to a 45% increase in energy dissipation per meter (across-shore) of a restored reef.

In a recent study, Roelvink et al. (2021) determined the optimal across-shore location for a coral reef restoration to mitigate coastal flooding is the upper fore reef or middle reef flat.

In their effort, the authors found that wave breaking on upper fore reef was the primary factor in reducing wave energy and coastal flooding. For the reef flat, where wave heights had already been diminished due to breaking at the reef crest, waves could be further dissipated through increases in bottom roughness via coral restoration. The results of the present study add a new dimensionality to this assessment, indicating that wave and turbulent energy dissipation is strongly controlled by incident wave height, period, and coral reef roughness. In terms of coral species, both Ghiasian et al. (2020) and Roelvink et al. (2021) suggest that restoration approaches consider fostering fast-growing corals such as *Acropora palmata* or *A. cervicornis* to rapidly increase bottom roughness and reduce wave heights over the reef. In particular, Ghiasian et al. (2020) found a 10% reduction in wave height, and a 14% reduction in wave energy, using models of *A. cervicornis* to simulate reef restoration. However, the selection of a specific species alone may not be enough to guarantee sufficient dissipation, particularly for reef systems where longer (in particular, infragravity) wave periods dominate. Further modeling of reef restorations under wave climates with longer periods is needed to determine the appropriate coral density to improve energy dissipation for these cases.

6 Conclusions

- Wave attenuation and energy dissipation scale with water depth and incident wave conditions, where greater attenuation and dissipation is expected for waves with shorter periods in shallower water.
- Near-bed turbulence scales negatively with water depth and positively with incident wave conditions.
- Relative to low relief corals (rugosity index =1.08), high relief corals (rugosity index = 1.24) generate greater turbulence above the bed under shorter wave periods (T_p = 4 – 12 s). Around T_p = 16 s, turbulence becomes less affected by bottom roughness as the ratio of the wave-orbital excursion to the scale of bottom roughness increases.
- Increasing the seabed roughness by at least 13% can result in enhanced wave attenuation and a 0.5 – 1.0 order of magnitude increase in turbulent energy dissipation, which translates to a 45% increase in energy dissipation per across-shore meter of restoration.
- Coastal managers planning restoration projects can utilize the information presented here to improve the dissipative characteristics of a degraded reef. For the water depths and incident wave conditions considered here, restorations are most valuable in shallow (1 – 2 m) depths under shorter period waves (T_p = 4 – 12 s).

7 Acknowledgements

This project was funded by the U.S. Geological Survey Coastal and Marine Hazards and Resources Program, the U.S. Geological Survey Mendenhall Research Fellowship Program, and the Australian-America Fulbright Commission. The authors would like to thank Babak Tehranirad (USGS) for their peer review of an earlier version of this manuscript and the anonymous reviewers for their considered feedback that made a valuable contribution to this study. The oceanographic timeseries, large-scale SfM, and fine-scale SfM data sets analyzed in this manuscript are available from USGS ScienceBase at https://doi.org/10.5066/P9FSG90O, https://doi.org/10.5066/P9XZT1FK, and https://doi.org/10.5066/P9HNLI7Y, respectively. Any use of trade, firm, or product names is for descriptive purposes only and does not imply endorsement by the U.S. Government.

References

Beck, M.W., Lange, G.M. (eds), 2016. Managing Coasts with Natural Solutions: Guidelines for Measuring and Valuing the Coastal Protection Services of Mangroves and Coral

Reefs. Washington D.C.

Burke, L., Reytar, K., Spalding, M., Perry, A., 2011. Reefs at risk revisited. World Resources Institute.

Cesar, H., Burke, L., Pet-Soede, L., 2003. The economics of worldwide coral reef degradation.

Cheriton, O.M., Storlazzi, C.D., Rosenberger, K.J., 2016. Observations of wave transformation over a fringing coral reef and the importance of low-frequency waves and offshore water levels to runup, overwash, and coastal flooding. J. Geophys. Res. Ocean. 121, 3121–3140. https://doi.org/10.1002/2015JC011231.Received

Dalrymple, R.A., Kirby, J.T., Hwang, P.A., 1984. Wave diffraction due to areas of energy dissipation. J. Waterw. Port, Coast. Ocean Eng. 110, 67–79. https://doi.org/10.1061/(ASCE)0733-950X(1984)110:1(67)

Davis, K.A., Pawlak, G., Monismith, S.G., 2021. Turbulence and Coral Reefs. Ann. Rev. Mar. Sci. 13, 343–373. https://doi.org/10.1146/annurev-marine-042120-071823

Devolder, B., Rauwoens, P., Troch, P., 2017. Application of a buoyancy-modified k- ω SST turbulence model to simulate wave run-up around a monopile subjected to regular waves using OpenFOAM ®. Coast. Eng. 125, 81–94.

Duvall, M.S., Hench, J.L., Rosman, J.H., 2019. Collapsing Complexity: Quantifying Multiscale Properties of Reef Topography. J. Geophys. Res. Ocean. 124, 5021–5038. https://doi.org/10.1029/2018JC014859

Fabian, R., Beck, M., Potts, D., 2013. Reef Restoration for Coastal Defense. Santa Cruz, CA, USA.

Ferrario, F., Beck, M.W., Storlazzi, C.D., Micheli, F., Shepard, C.C., Airoldi, L., 2014. The effectiveness of coral reefs for coastal hazard risk reduction and adaptation. Nat. Commun. 5, 1–9. https://doi.org/10.1038/ncomms4794

Ghiasian, M., Carrick, J., Rhode-Barbarigos, L., Haus, B., Baker, A.C., Lirman, D., 2020. Dissipation of wave energy by a hybrid artificial reef in a wave simulator: implications for coastal resilience and shoreline protection. Limnol. Oceanogr. Methods. https://doi.org/10.1002/lom3.10400

Gon, C.J., Macmahan, J.H., Denny, M., 2020. Wave Dissipation by Bottom Friction on the Inner Shelf of a Rocky Shore. J. Geophys. Res. Ocean. 125. https://doi.org/10.1029/2019JC015963

Gourlay, M.R., 1994. Wave transformation on a coral reef. Coast. Eng. 23, 17–42.

Harris, Daniel L., Rovere, A., Casella, E., Power, H., Canavesio, R., Collin, A., Pomeroy, A., Webster, J.M., Parravicini, V., 2018. Coral reef structural complexity provides important coastal protection from waves under rising sea levels. Sci. Adv. 4, 1–8. https://doi.org/10.1126/sciadv.aao4350

Harris, Daniel L, Rovere, A., Casella, E., Power, H., Canavesio, R., Collin, A., Pomeroy, A., Webster, J.M., Parravicini, V., 2018a. Coral reef structural complexity provides important coastal protection from waves under rising sea levels 1–8.

Harris, Daniel L, Vila-concejo, A., Power, H.E., Kinsela, M.A., Webster, J.M., 2018b. Estuarine , Coastal and Shelf Science Variability of depth-limited waves in coral reef surf zones. Estuar. Coast. Shelf Sci. 211, 36–44. https://doi.org/10.1016/j.ecss.2018.06.010

Hench, J.L., Rosman, J.H., 2013. Observations of spatial flow patterns at the coral colony scale on a shallow reef flat. J. Geophys. Res. Ocean. 118, 1142–1156. https://doi.org/10.1002/jgrc.20105

Higuera, P., Lara, J.L., Losada, I.J., 2013. Realistic wave generation and active wave absorption for Navier-Stokes models. Application to OpenFOAM®. Coast. Eng. 71, 102–118. https://doi.org/10.1016/j.coastaleng.2012.07.002

Hirt, C.W., Nichols, B.D., 1981. Volume of Fluid (VOF) Method for the Dynamics of Free Boundaries. J. Comput. Phys. 39, 201–225. https://doi.org/https://doi.org/10.1016/0021-9991(81)90145-5

Huang, Z.C., Lenain, L., Melville, W.K., Middleton, J.H., Reineman, B., Statom, N., McCabe, R.M., 2012. Dissipation of wave energy and turbulence in a shallow coral reef lagoon. J. Geophys. Res. Ocean. 117, 1–18. https://doi.org/10.1029/2011JC007202

Jaramillo, S., Pawlak, G., 2011. AUV-based bed roughness mapping over a tropical reef. Coral Reefs 30, 11–23. https://doi.org/10.1007/s00338-011-0731-9

Larsen, B.E., Fuhrman, D.R., 2018. On the over-production of turbulence beneath surface waves in Reynolds-averaged Navier-Stokes models. J. Fluid Mech. 853, 419–460. https://doi.org/10.1017/jfm.2018.577

Le Méhauté, B., 1967. An Introduction to Hydrodynamics and Water Waves. Springer, Berlin, Heidelberg.

Lentz, S.J., Churchill, J.H., Davis, K.A., Farrar, J.T., 2016. Surface Gravity Wave Transformation across a Platform Coral Reef in the Red Sea. J. Geophys. Res. Ocean. 121, 693–705. https://doi.org/10.1002/2015JC011142.Received

Logan, J. and Storlazzi, C.D., 2021. Aerial Imagery and Structure-from-Motion Derived Shallow Water Bathymetry from UAS Survey of the Coral Reef off Waiakane, Molokai, HI June 2018. U.S. Geological Survey Data Release. https://doi.org/10.5066/P9XZT1FK

Longuet-Higgins, M.S., Fenton, J.., 1974. On the Mass, Momentum, Energy and Circulation of a Solitary Wave. II, in: Proceedings of the Royal Society of London. Series A, Mathematical and Physical Sciences. Royal Society, London, UK, pp. 471–493.

Lowe, R.J., Buckley, M.L., Altomare, C., Rijnsdorp, D.P., Yao, Y., Suzuki, T., Bricker, J.D., 2019. Numerical simulations of surf zone wave dynamics using Smoothed Particle Hydrodynamics. Ocean Model. 144, 101481. https://doi.org/10.1016/j.ocemod.2019.101481

Lowe, R.J., Falter, J.L., Bandet, M.D., Pawlak, G., Atkinson, M.J., Monismith, S.G., Koseff, J.R., 2005. Spectral wave dissipation over a barrier reef. J. Geophys. Res. C Ocean. 110, 1–16. https://doi.org/10.1029/2004JC002711

Luhar, M., Infantes, E., Orfila, A., Terrados, J., Nepf, H.M., 2013. Field observations of wave-induced streaming through a submerged seagrass (Posidonia oceanica) meadow. J. Geophys. Res. Ocean. 118, 1955–1968. https://doi.org/10.1002/jgrc.20162

Madsen, O.S., Poon, Y., Graber, H.C., 1988. Spectral Wave Attenuation. Coast. Eng. 492–504.

Monismith, S.G., Rogers, J.S., Koweek, D., Dunbar, R.B., 2015. Frictional wave dissipation on a remarkably rough reef. Geophys. Res. Lett. 42, 4063–4071. https://doi.org/10.1002/2015GL063804

Montgomery, E.M., Martini, M.A., Lightsom, F.L., Butman, B., Nowacki, D.J., Suttles, S.E., 2008. Documentation of the U.S. Geological Survey Oceanographic Time-Series Measurement Database (ver. 3.0, April 2021). U.S. Geological Survey Open-File Report 2007–1194. https://doi.org/https://doi.org/10.3133/ofr20071194

Nelson, R.C., 1994. Depth limited design wave heights in very flat regions. Coast. Eng. 23, 43–59.

Nielsen, P., 1992. Coastal Bottom Boundary Layers and Sediment Transport. World Scientific Publishing Company, Singapore. https://doi.org/10.1142/1269

Norris, B.K., Mullarney, J.C., Bryan, K.R., Henderson, S.M., 2019. Turbulence Within Natural Mangrove Pneumatophore Canopies. J. Geophys. Res. Ocean. 124, 2263–2288. https://doi.org/10.1029/2018JC014562

Ogston, A.S., Storlazzi, C.D., Field, M.E., Presto, M.K., 2004. Sediment resuspension and transport patterns on a fringing reef flat, Molokai, Hawaii. Coral reefs 23, 559–569.

OpenFOAM, 2020. OpenFOAM User’s Guide.

Perry, C.T., Murphy, G.N., Graham, N.A.J., Wilson, S.K., Januchowski-Hartley, F.A., East, H.K., 2015. Remote coral reefs can sustain high growth potential and may match future sea-level trends. Sci. Rep. 5, 18289.

Pizarro, O., Friedman, A., Bryson, M., Williams, S.B., Madin, J., 2017. A simple, fast, and repeatable survey method for underwater visual 3D benthic mapping and monitoring. Ecol. Evol. 7, 1770–1782. https://doi.org/10.1002/ece3.2701

Pomeroy, A., Lowe, R., Symonds, G., Van Dongeren, A., Moore, C., 2012. The dynamics of infragravity wave transformation over a fringing reef. J. Geophys. Res. Ocean. 117, 1–17. https://doi.org/10.1029/2012JC008310

Pomeroy, A., Storlazzi, C.D., Logan, J. and Norris, B.K., 2022. Fine-scale Structure-from-Motion of Low and High Relief Sites from the Coral Reef Flat off Waiakane, Molokai, HI. U.S. Geological Survey Data Release. https://doi.org/10.5066/P9HNLI7Y

Quataert, E., Storlazzi, C., Rooijen, A., Cheriton, O., Dongeren, A., 2015. The influence of coral reefs and climate change on wave-driven flooding of tropical coastlines 1–9. https://doi.org/10.1002/2015GL064861.Received

Reidenbach, M.A., Stocking, J.B., Szczyrba, L., Wendelken, C., 2021. Hydrodynamic interactions with coral topography and its impact on larval settlement. Coral Reefs 40, 505–519. https://doi.org/10.1007/s00338-021-02069-y

Rosenberger, K.J., Storlazzi, C.D., Cheriton, O.M., and Logan, J.B., 2019, Waiakane, Molokai, HI, 2018 Coral Reef Circulation and Sediment Dynamics Experiment: U.S. Geological Survey Data Release. https://doi.org/10.5066/P9FSG90O.

Sous, D., Dodet, G., Bouchette, F., Tissier, M., 2020. Momentum Balance Across a Barrier Reef. J. Geophys. Res. Ocean. 125. https://doi.org/10.1029/2019JC015503

Spalding, M., Burke, L., Wood, S.A., Ashpole, J., Hutchison, J., zu Ermgassen, P., 2017. Mapping the global value and distribution of coral reef tourism. Mar. Policy 82, 104–113. https://doi.org/10.1016/j.marpol.2017.05.014

Storlazzi, C.D., Logan, J.B., Field, M.E., 2003. Quantitative morphology of a fringing reef tract from high-resolution laser bathymetry: Southern Molokai, Hawaii. Bull. Geol. Soc. Am. 115, 1344–1355. https://doi.org/10.1130/B25200.1

Storlazzi, C.D., Norris, B.K., Rosenberger, K.J., 2015. The influence of grain size, grain color, and suspended-sediment concentration on light attenuation: Why fine-grained terrestrial sediment is bad for coral reef ecosystems. Coral Reefs. https://doi.org/10.1007/s00338-015-1268-0

Swart, D.H., 1974. Offshore Sediment Transport and Equilibrium Beach Profiles. TU Delft.

Thornton, E.B., Guza, R.T., 1982. Energy Saturation and Phase Speeds Measured on a Natural Beach. J. Geophys. Res. 87, 9499–9508.

Van der Westhuysen, A.J., 2010. Modeling of depth-induced wave breaking under finite depth wave growth conditions. J. Geophys. Res. Ocean. 115, 1–19. https://doi.org/10.1029/2009JC005433

Vyzikas, T., Stagonas, D., Buldakov, E., Greaves, D., 2018. The evolution of free and bound waves during dispersive focusing in a numerical and physical fl ume. Coast. Eng. 132, 95–109. https://doi.org/10.1016/j.coastaleng.2017.11.003

Wen, H., Ren, B., Dong, P., Zhu, G., 2020. Numerical analysis of wave-induced current within the inhomogeneous coral reef using a refined SPH model. Coast. Eng. 156, 103616. https://doi.org/10.1016/j.coastaleng.2019.103616

Wiberg, P.L., Sherwood, C.R., 2008. Calculating wave-generated bottom orbital velocities from surface-wave parameters. Comput. Geosci. 34, 1243–1262. https://doi.org/10.1016/j.cageo.2008.02.010

Wiles, P.J., Rippeth, T.P., Simpson, J.H., Hendricks, P.J., 2006. A novel technique for measuring the rate of turbulent dissipation in the marine environment. Geophys. Res. Lett. 33, L21608. https://doi.org/10.1029/2006GL027050

Woodroffe, C.D., Webster, J.M., 2014. Coral reefs and sea-level change. Mar. Geol. 352, 248–267.

Young, C.N., Schopmeyer, S.A., Lirman, D., 2012. A review of reef restoration and coral propagation using the threatened genus Acropora in the Caribbean and Western Atlantic. Bull. Mar. Sci. 88, 1075–1098.

Table 1: Aggregation of literature and field observation values for hydrodynamic conditions over reef flats from coral reefs worldwide.

Reference	Location	h (min) max	H_s (min) max	T_p (min) max
Hardy et al., (1990)	John Brewer Reef, Australia	-	(0.2) 1.3	(0.5) 2.6
Sulaiman et al., (1994)	Sanur Beach, Bali	(0) 0.5	(0.15) 0.3	(3) 4.5
Brander et al., (2004)	Warraber Island, Australia	(0.4) 2.0	(0.1) 0.5	(1.3) 8.0
Lowe et al., (2005)	Kaneohe Bay, Hawai‘i	(0.4) 1.1	(0.1) 0.7	(6.0) 14.0
Lentz et al., (2015)	Red Sea	(0.3) 1.2	(0) 1.2	(4.0) 8.0
Cheriton et al., (2016)	Roi-Namur Island, Marshall Islands	(0) 1.4	(0.3) 0.5	(8.0) 18.0
Beetham et al., (2016)	Funafuti Atoll, Tuvalu	(0) 0.8	(0.5) 1.8	(10.0) 15.0
Harris et al., (2018b)	One Tree Reef, Australia	(0.1) 3.6	(0.1) 1.0	(6.0) 18.0
Pomeroy et al., (2019)	Moloka‘i, Hawai‘i	(1.2) 2.0	(0.1) 0.6	(10.9) 18.3
Rosenberger, Cheriton & Storlazzi (2021)	Kwajalein Island, Marshall Islands	(0.2) 1.6	(0) 0.8	(12.0) 18.0
Rosenberger, Cheriton & Storlazzi (2021)	Roi-Namur Island, Marshall Islands	(0.7) 2.2	(0) 0.5	(4.0) 16.0
Rosenberger, Cheriton & Storlazzi (2021)	Maui, Hawai‘i	(2.5) 3.6	(0.3) 1.5	(8.3) 17.0

Table 2: Model scenarios based on literature values and observation data (Table 1) for four water depths (h), five significant wave heights (H_s) and peak wave periods (T_p). Scenarios with unrealistic combinations of conditions (where $H_s/h \geq 0.73$ and $H_s/\lambda \geq 0.142$) were eliminated.

	H_s	0.4					0.8					1.2					1.6					2.0				
h	T_p	**4**	**8**	**12**	**16**	**20**	**4**	**8**	**12**	**16**	**20**	**4**	**8**	**12**	**16**	**20**	**4**	**8**	**12**	**16**	**20**	**4**	**8**	**12**	**16**	**20**
1.0	Case ID	1	2	3	4	5																				
2.0		6	7	8	9	10	11	12	13	14	15	16	17	18	19	20										
3.0		21	22	23	24	25	26	27	28	29	30	31	32	33	34	35	36	37	38	39	40	41	42	43	44	45
4.0		46	47	48	49	50	51	52	53	54	55	56	57	58	59	60	61	62	63	64	65	66	67	68	69	70

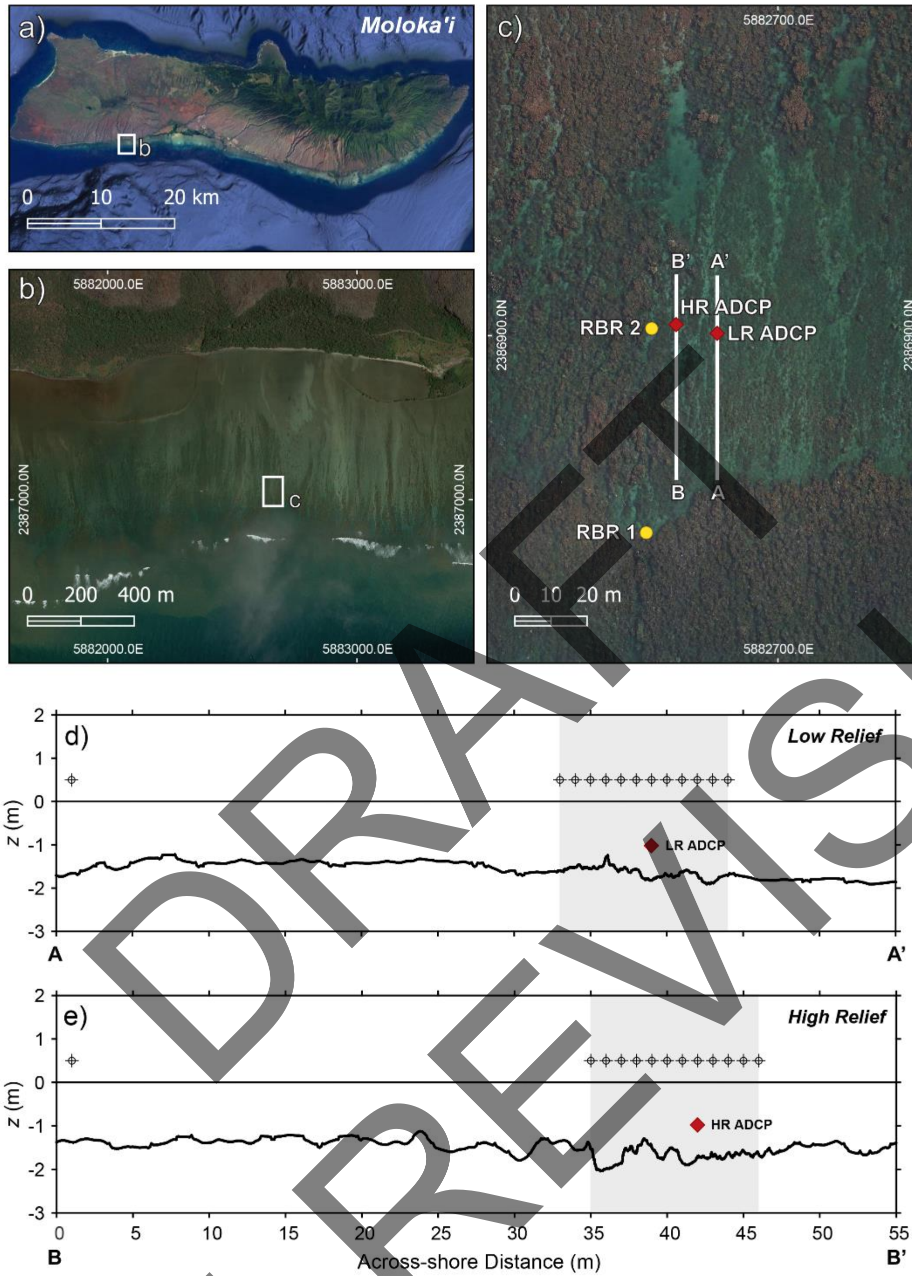

Figure 1: Morphology of the study area off Moloka‘i, Hawai‘i, and the location of instruments used in model calibration and validation. (a – c) Map of deployment locations. (c) Location of instrument deployments and orientation of cross-sections used in numerical models. (d – e) Bathymetric profiles for Low (d) and High (e) Relief study sites, with fine-scale survey areas delineated by shaded areas. Symbols (⊕) above the still water level (z = 0 m) denote the across-shore locations of digital wave gauges. In (c – e), “LR” refers to the Low Relief site instrument, “HR” the High Relief site instrument, and “ADCP” the Nortek Aquadopps.

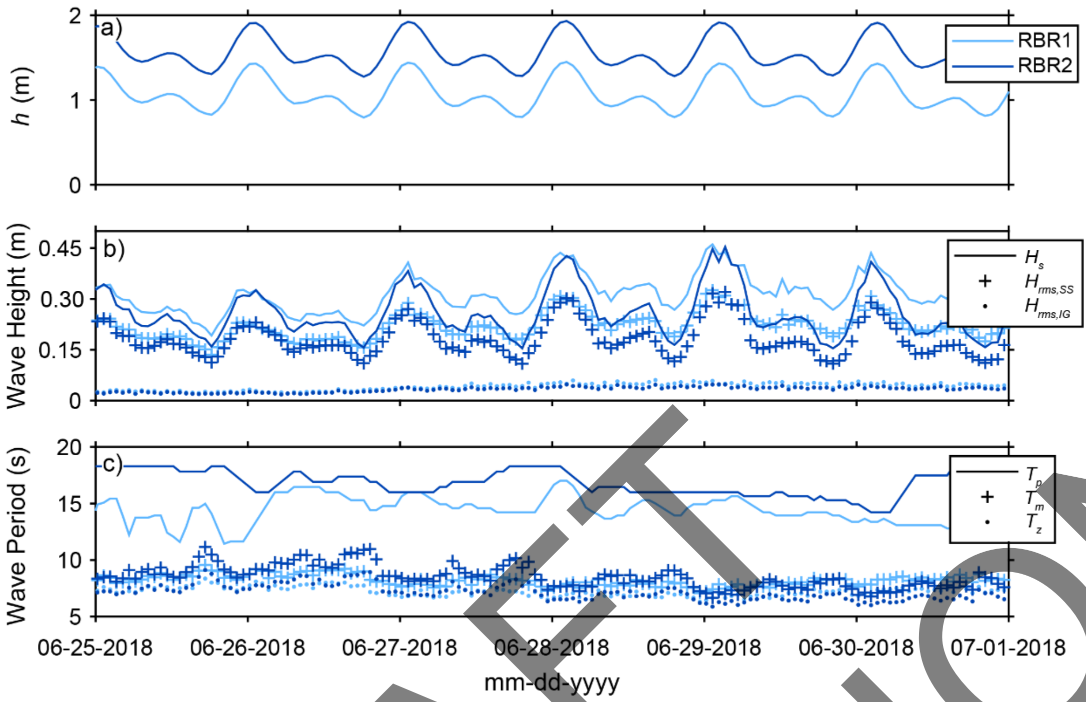

Figure 2: Observed burst-averaged conditions during and after the model calibration period (25-26 June 2018) along the model transects between RBR1 and RBR2 spaced ~55 m apart in the across-shore direction. (a) Water depth. (b) Wave height. (c) Wave period. During the calibration period, the sea-swell RMS wave height ($H_{rms,SS}$) greatly exceeded the infragravity wave height ($H_{rms,IG}$); both were modulated by water depth.

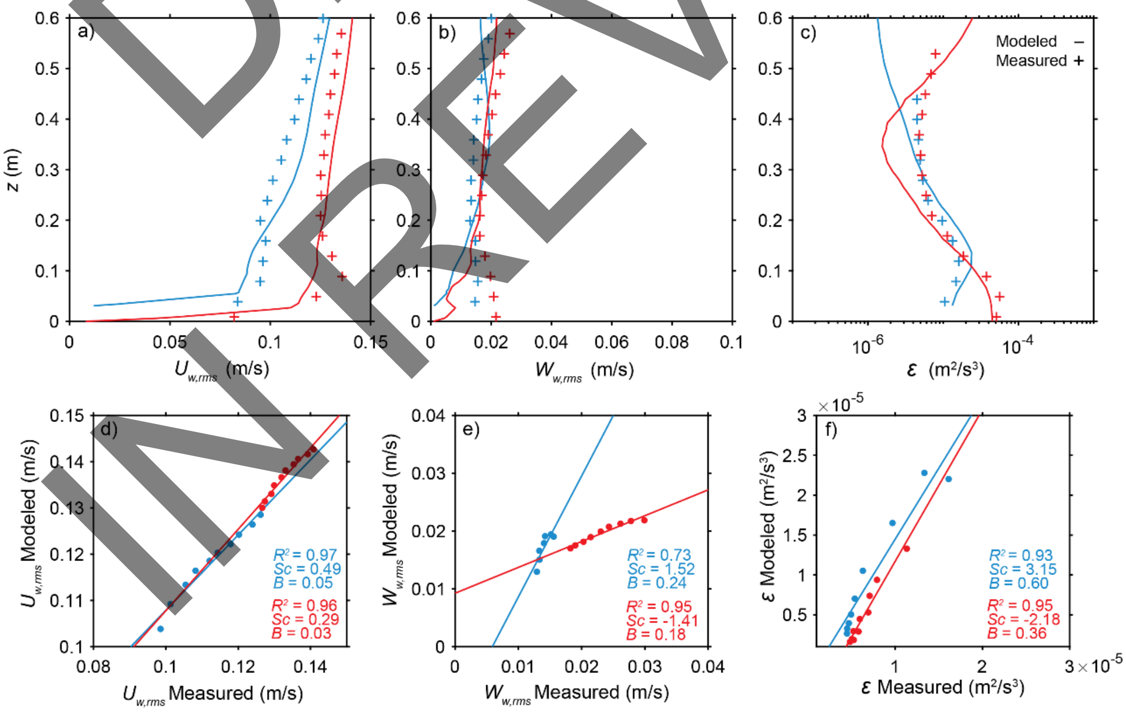

Figure 3: Comparison of field measurements to numerical model results during the calibration period. Depth profiles of (a) cross-shore root-mean-squared wave velocity, $U_{w,rms}$. (b) vertical root-mean squared wave velocity, $W_{w,rms}$. and (c) *TKE* dissipation rate, ε, comparing observations (symbols) to model results (lines). Linear regressions between observations and model results, with goodness-of-fit (R^2), scatter (*Sc*), and bias (*B*) indices for (d) cross-shore root-mean-squared wave velocity, $U_{w,rms}$. (e) vertical root-mean squared wave velocity, $W_{w,rms}$. and (f) *TKE* dissipation rate, ε,. For all subplots, blue is the Low Relief case and red the High Relief case. Note the field data are well represented by the models.

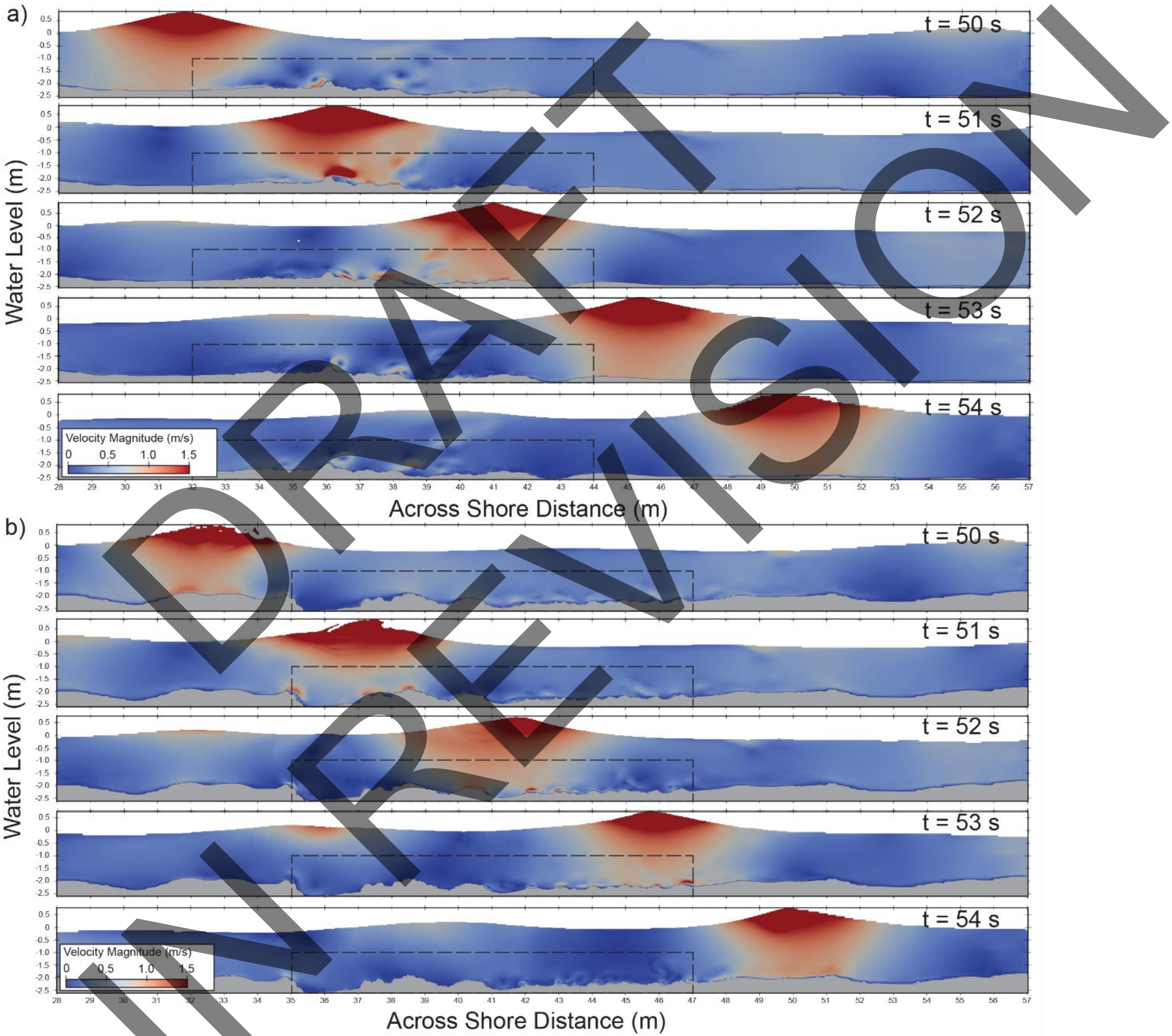

Figure 4: Timeseries of wave propagation along the (a) Low Relief model domain and (b) High Relief model domain for timesteps t = 50 – 54 s. The dashed area in each domain indicates the high-resolution area "the patch" of each model grid. In this area, vortices spin off the rough bathymetry as the wave crest passes overhead.

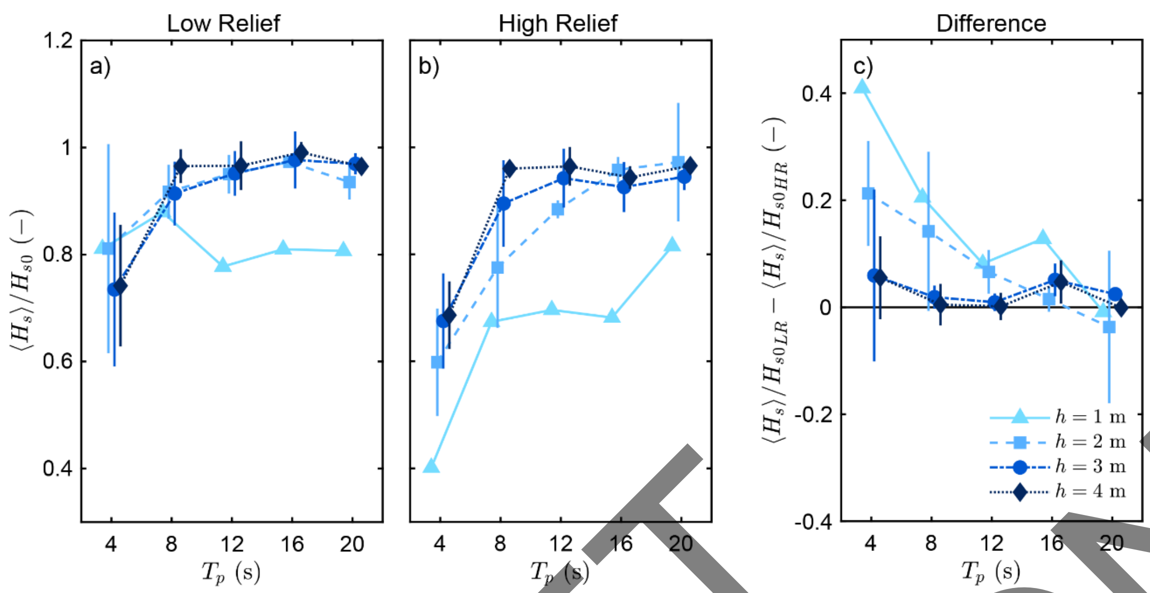

Figure 5: Wave attenuation across the (a) Low Relief and (b) High Relief patches, represented by the ratio of the spatial mean significant wave height $\langle H_s \rangle$ and the significant wave height at the model inlet (H_{s0}); the differences between the Low Relief and High Relief scenarios are presented in (c). Results are presented for all model scenarios at four water depths (h = 1 – 4 m). Data points display the mean and one standard deviation and have been slightly offset at each value of T_p for display purposes. Note the greater wave attenuation across the higher relief patch, especially for shorter wave periods.

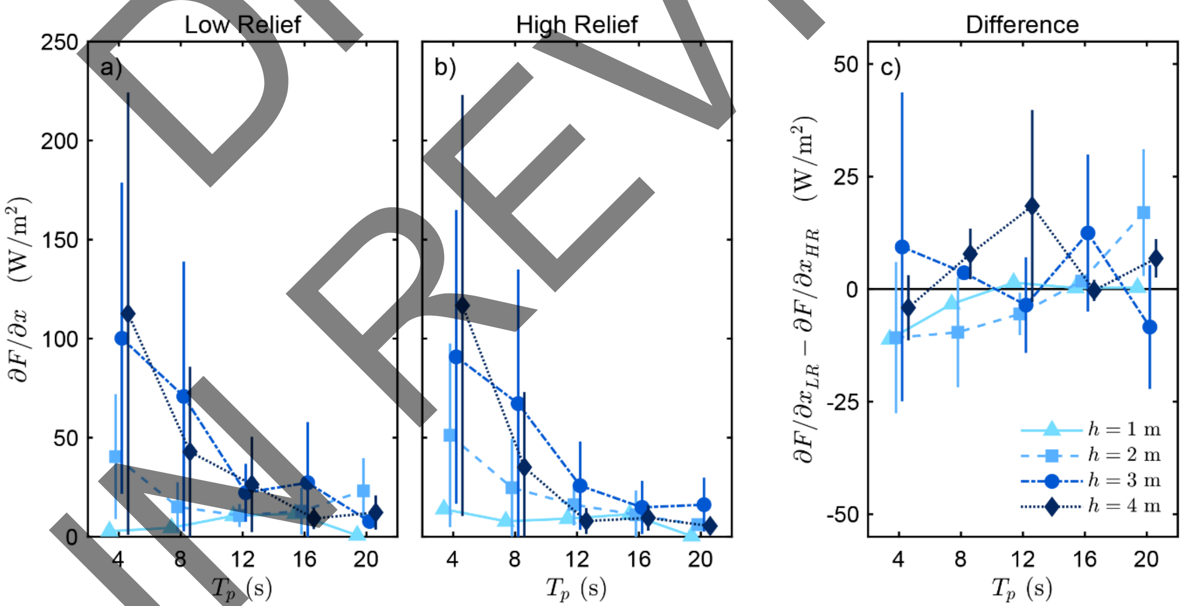

Figure 6: Wave energy dissipation from the model inlet across the (a) Low Relief and (b) High Relief patch areas under four water depths (h = 1 – 4 m) for all model scenarios; the differences between the Low Relief and High Relief scenarios are presented in (c). Data points display the mean and one standard deviation and have been slightly offset at each value of T_p for display purposes. Note the general trend of greater wave energy dissipation for shorter wave periods.

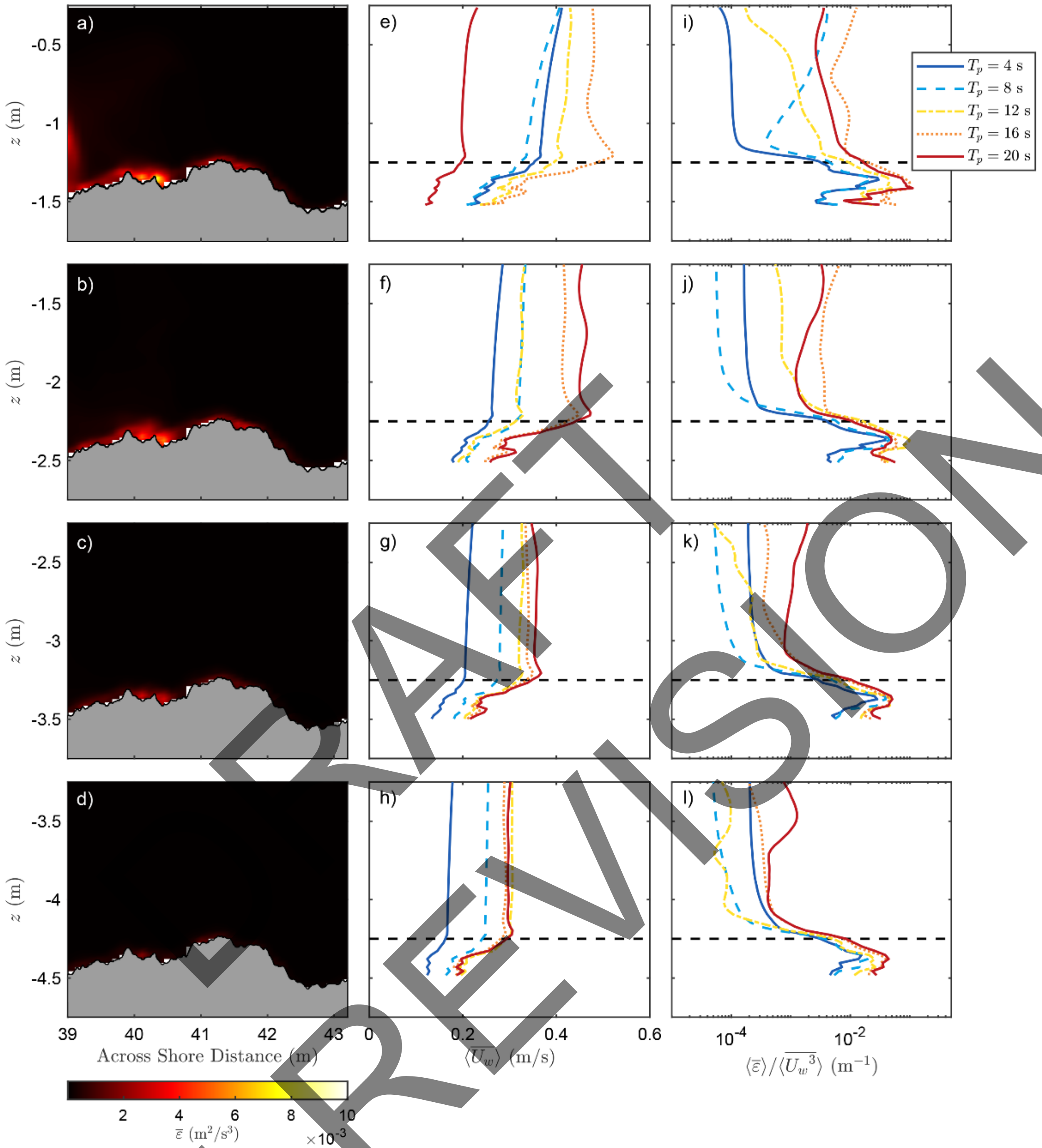

Figure 7: Modeled turbulence (ε) and wave velocities (U_w) for Low Relief scenarios with h = 1 – 4 m and T_p = 4 – 20 s at a constant H_s = 0.4 m. (a – d) Time averaged *TKE* dissipation ($\bar{\varepsilon}$) for a subsection of the Low Relief patch for T_p = 12 s waves. (e – f) Depth profile of time and space mean wave velocity $\langle \overline{U_w} \rangle$. (i – l) Depth profile of time and space mean normalized *TKE* dissipation $\langle \bar{\varepsilon} \rangle$ by the mean wave velocity cubed $\langle \overline{U_w{}^3} \rangle$. The dashed line in e – l denotes the top of the bed roughness in a – c. Note the inflection point in the profiles in e – l corresponds to the top of the bed roughness.

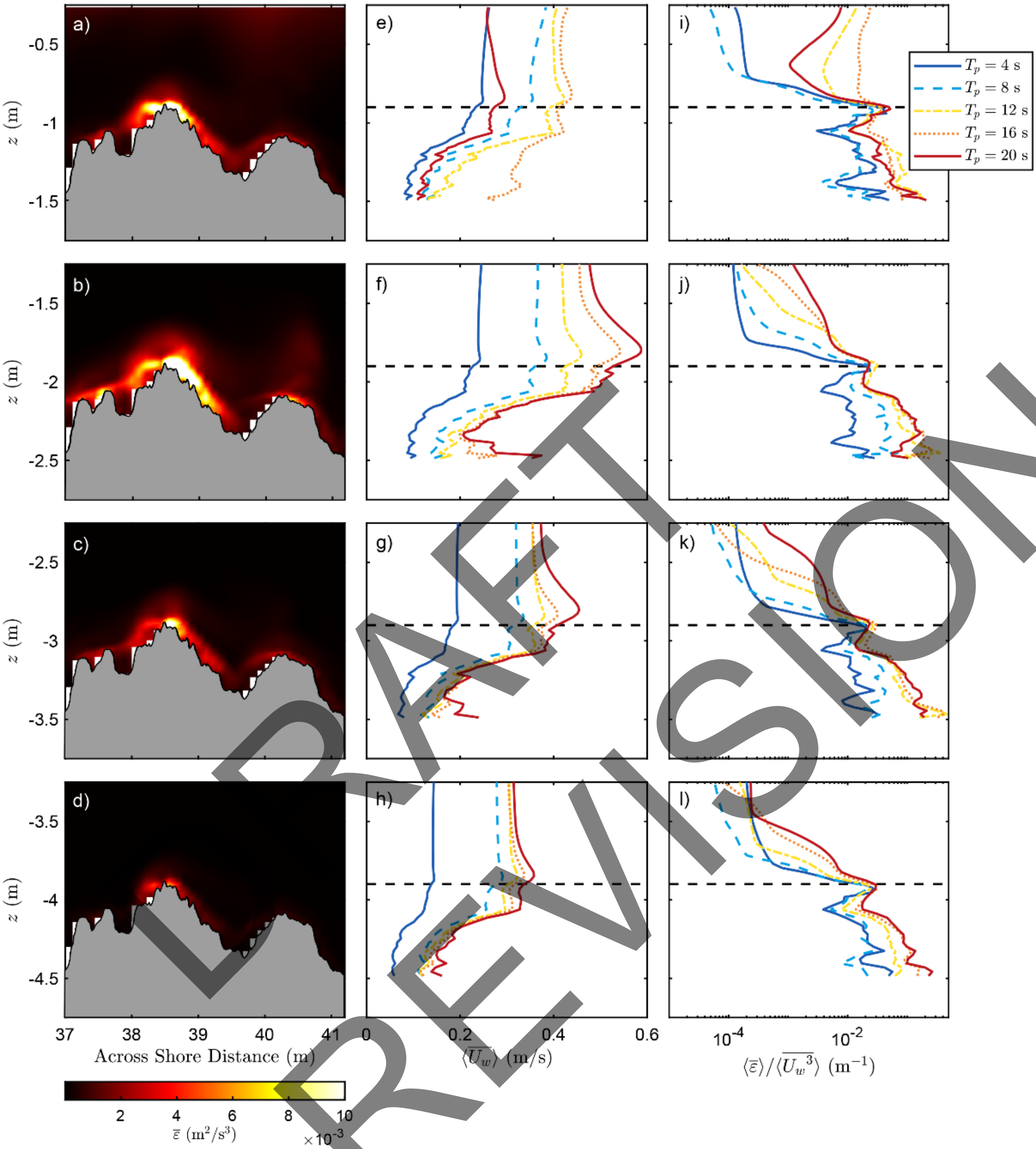

Figure 8: Modeled turbulence (ε) and wave velocities (U_w) for High Relief scenarios with h = 1 – 4 m and T_p = 4 – 20 s at a constant H_s = 0.4 m. (a – d) Time averaged *TKE* dissipation ($\bar{\varepsilon}$) for a subsection of the High Relief patch for T_p = 12 s waves. (e – f) Depth profile of time and space mean wave velocity $\langle \overline{U_w} \rangle$. (i – l) Depth profile of time and space mean normalized *TKE* dissipation $\langle \bar{\varepsilon} \rangle$ by the mean wave velocity cubed $\langle \overline{U_w{}^3} \rangle$. Dashed line in e – l denotes the top of the bed roughness in a – c. Note the inflection point in the profiles in e – l corresponds to the top of the bed roughness, both of which are higher above the seabed than in Figure 7.

875

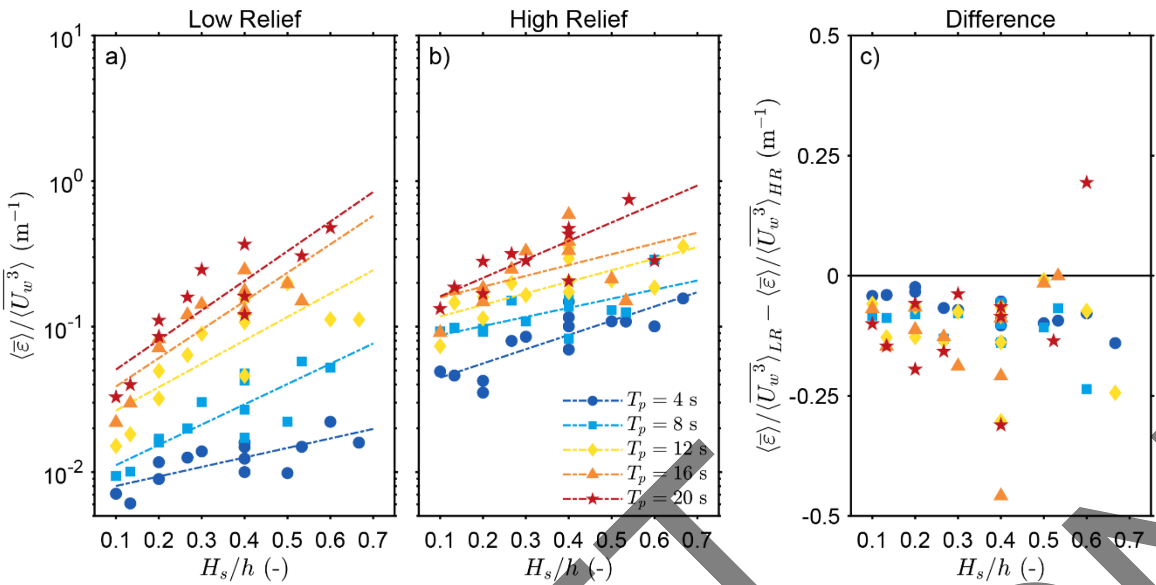

Figure 9: Comparison of mean normalized *TKE* dissipation for all (a) Low and (b) High Relief scenarios against the wave breaking parameter $\gamma = H_s/h$; the differences between the Low Relief and High Relief scenarios are presented in (c). Colors and symbols indicate the different wave periods (T_p = 4 – 20 s), and dashed lines are log-linear fits to the data to depict trends. Note the trends in greater dissipation for larger wave heights but less difference between the Low Relief and High Relief scenarios for longer wave periods.

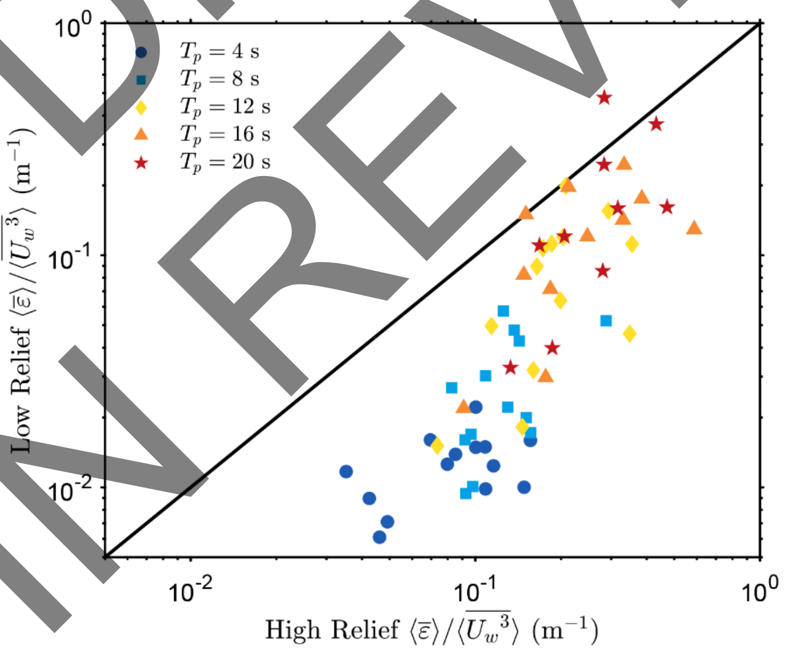

Figure 10: Normalized turbulence for all Low and High Relief scenarios. Colors and symbols indicate the different wave periods (T_p = 4 – 20 s). The thick diagonal line is unity. Points that lie below the line indicate greater turbulence across the High Relief patch, whereas points that lie above the line indicate greater turbulence across the Low Relief patch. There is nearly one order of magnitude difference between the Low and High Relief cases for shorter wave periods, but this difference becomes less significant with increasing wave period.

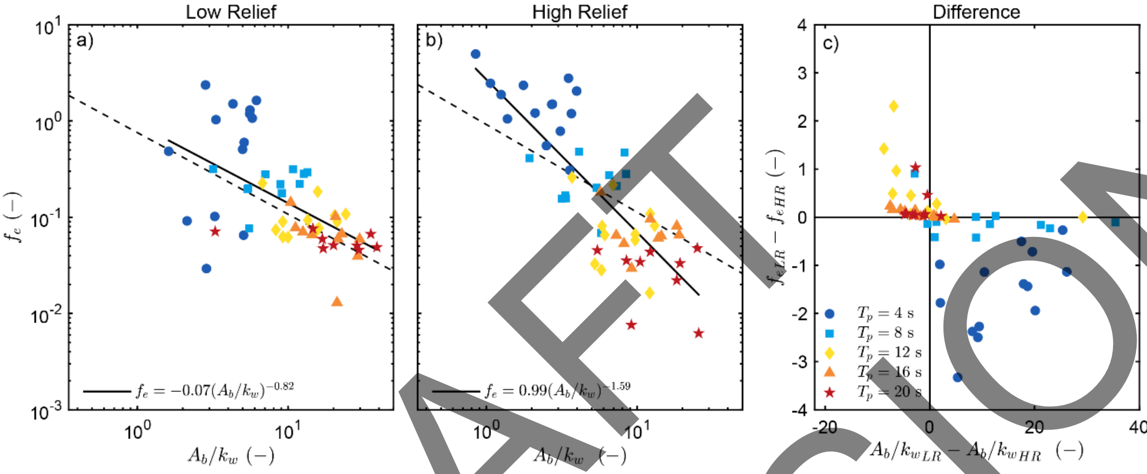

Figure 11: Wave energy dissipation factors f_e, representing the rate of conversion of wave motion into turbulence, as a function of A_b/k_w for the (a) Low and (b) High Relief scenarios; the differences between the Low Relief and High Relief scenarios are presented in (c). Colors and symbols indicate the different wave periods (T_p = 4 – 20 s). The dashed black line is Eq. (5) (Nielsen 1992), and the solid black line is the power fit to the data as indicated in each plot legend. In (a) and (b), the High Relief cases have a greater slope than the Low Relief cases, implying that the conversion of wave momentum into turbulence occurs at a faster rate over rougher surfaces. Note in (c), negative values of the difference between Low and High Relief cases for T_p = 4 – 8 s suggests greater energy dissipation over High Relief bathymetry mainly occurs during shorter wave periods.

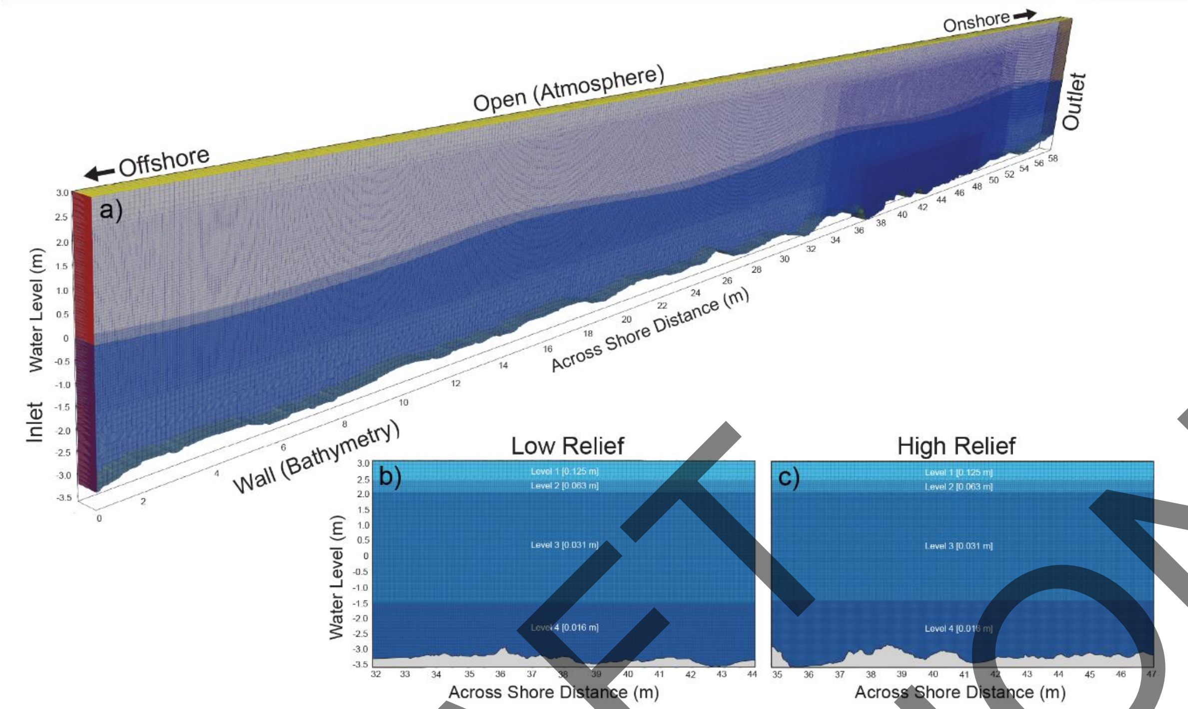

Figure S1: Model grid layout for the calibration cases. (a) Orthographic layout of the High Relief calibration mesh, with boundaries as colors and model boundary conditions listed. (b) The fine-scale patch area of the Low Relief model. (c) The fine-scale patch area of the High Relief model. In (b – c), shades represent cell sizes in terms of levels of mesh refinement: Level 0: 0.25 m; Level 1: 0.125 m; Level 2: 0.063 m; Level 3: 0.031 m; Level 4: 0.016 m.

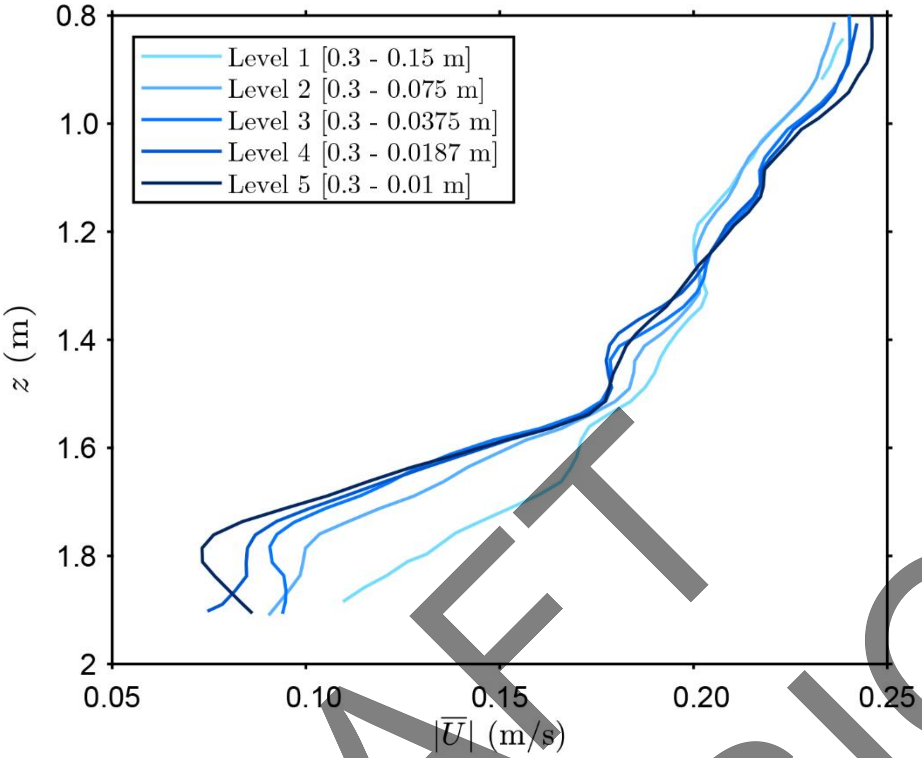

Figure A.1: The effect of model mesh refinement on the magnitude of the near-bed mean velocity magnitude, $|\bar{U}|$. Mesh sizes ranged from 0.3 m at the largest to 0.01 m at the smallest, corresponding to Levels 1 through 5 refinement, respectively. This test of mesh refinement was used to determine at which point the model results were grid-independent (the profiles converge), which occurs at “Level 3” refinement and above.

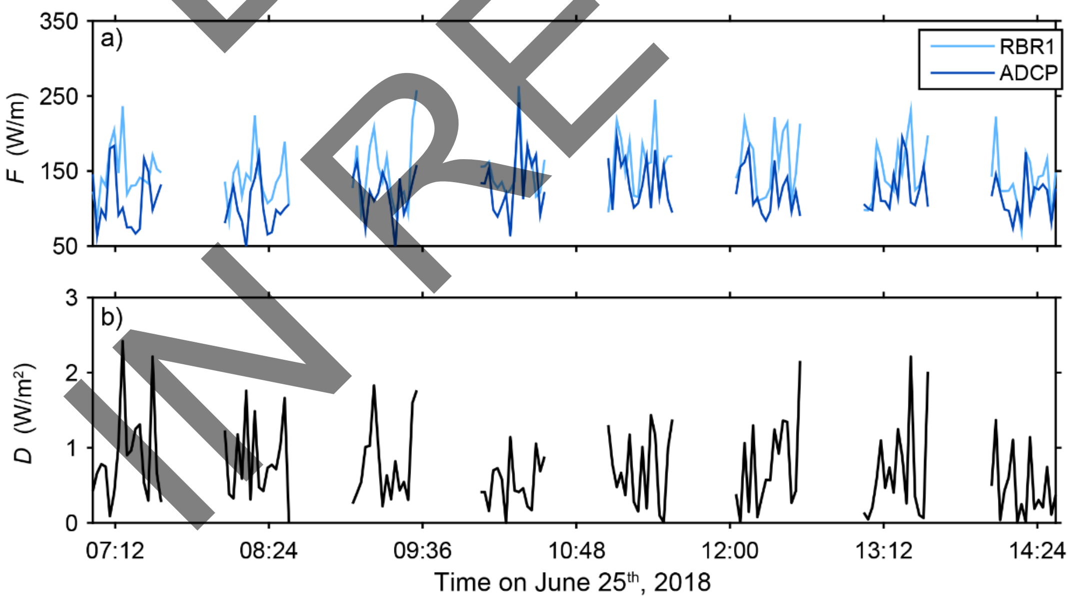

Figure A.2: (a) A comparison of wave energy flux (F) and (b) wave energy dissipation (D) between the upstream RBR1 and the ADCP at the High Relief site during the model calibration period on 25 June 2018.

Nomenclature

A_b	wave orbital excursion.
a	wave amplitude.
C_g	wave group velocity.
C_o	Courant number.
E	total wave energy.
F	wave energy flux.
f_e	wave energy dissipation factor.
g	gravitational constant (= 9.81 m/s^2).
H	wave height.
H_s	significant wave height.
H_{s0}	incident significant wave height.
h	water depth.
j	the *j-th* frequency component of a spectrum.
k	wavenumber.
k_w	bottom roughness.
p^*	modified pressure after removing hydrostatic.
r	a representative value.
rms	root-mean-square.
S_η	water surface elevation spectrum.
t	time.
T	wave period.
T_p	peak wave period.
T_m	mean wave period.
T_z	zero-crossing wave period.
u_b	near-bottom orbital velocity.
U	velocity magnitude.
U_c	horizontal (current) velocity.
U_w	oscillatory (wave) velocity.
x	across-shore distance.
z^+	wall distance function.

α fluid phase term (air: $\alpha = 0$; water: $\alpha = 1$).

β wave direction.

Δf spectral bandwidth.

Δx model cell size in the direction of the velocity.

ε turbulent kinetic energy dissipation rate.

ε_b wave dissipation due to breaking.

ε_b wave dissipation due to bottom friction.

γ critical wave breaking parameter.

κ_c interface curvature (of the free surface).

λ wavelength.

μ_{eff} effective dynamic viscosity.

ω wave radian frequency.

ρ water density (= 1025 kg/m^3).

ψ wave phase.

σ_r the standard deviation of a bathymetric profile.

σ_T surface tension coefficient (=0.07 kg/s^2).

$\overline{}$ temporal averaging operator.

$\langle\,\rangle$ spatial averaging operator.

Appendix A: Model mesh scale calibration

A numerical solution is determined to be grid-scale independent if the difference between two consecutive solutions is negligible after refining the grid. For the calibration step, grid-scale independence was assessed with a series of five models using the High Relief model domain, each varying the degree of grid cell resolution, from coarse ($\Delta x = 0.3 – 0.15$ m) to very fine ($\Delta x = 0.3 – 0.01$ m) scales. Grid cell refinement levels were specified in snappyHexMesh as different integers (Level 1, 2, 3…) within the region of the mesh containing the free surface and in the fine-scale patch area of the model domain. During meshing, snappyHexMesh first splits the cells in the background mesh that intersect with the bathymetry. Mesh refinement occurs along this boundary and several layers of cells are formed by subdividing the initial mesh to the specified refinement level. Cells below the bathymetry are removed, and cells intersecting the bathymetry are snapped to the surface. Hence, greater refinement levels produce greater resolution of bathymetric features due to a smaller cell size near the boundary.

Each refinement model was run with identical forcing conditions and model settings as described in Section 3.6.2. Model runs consisted of 512 s with a 64 s spin-up time and a sampling period that lasted roughly ten wave cycles. Models were sampled using a volume containing only the fine-scale patch area of the mesh. Profiles of the mean velocity magnitude $|\overline{U}|$ were computed by averaging over the patch width and in time. In Figure A.1, the depth profiles of $|\overline{U}|$ converge at Level 3 refinement and above, indicating grid-size independent results.

In addition, the grid refinement models were also calibrated with the total observed wave energy dissipation during a subsection of the calibration window when waves were relatively large. With this analysis, it was assumed that all energy dissipation within the fine-scale patch area of the model domain was due to bottom friction, and hence was equivalent to the wave energy dissipation (Eq. 2). The wave energy flux and dissipation were calculated between the RBR1 pressure transducer and the High Relief site ADCP. The mean wave energy flux and dissipation were computed from time-synchronized pressure measurements using a windowed time series with 300 s segments using a 30% overlap between segments over each burst. The total wave energy dissipation rate, hereafter *D*, is estimated from the spatial gradient of the measured wave energy flux *F* using a modified form of Eq. (2) (e.g., Huang et al. 2012),

$$D = -\frac{\Delta F}{\Delta x \cdot \cos\theta} \tag{A.1}$$

where Δx is the distance between two adjacent measurement sites (= 55 m) and θ is the angle of the wave propagation relative to the line intersecting the two instruments. The wave energy flux in each frequency band *j* can be expressed as

$$F_j = \frac{1}{2}\rho g {a_j}^2 C_{g,j} \tag{A.2}$$

where ρ is the water density (= 1025 kg/m^3), g is the gravitational constant (= 9.81 m/s^2), and $C_{g,j}$ the wave group velocity. Following Dalrymple et al., (1984) $C_{g,j}$ is estimated as

$$C_{g,j} = \frac{1}{2}\left(1 + \frac{2k_j h}{\sinh 2k_j h}\right)\left[\left(\frac{g}{k_j}\right)\tanh k_j h\right]^{1/2} \tag{A.3}$$

where *k* is the wavenumber ($= 2\pi/\lambda$, where λ is the wavelength calculated from the linear wave theory dispersion relation) and *h* is the burst-mean water depth. The total energy flux *F* was determined by summing (A.2) across the frequency band spanning 0.001 and 0.3 Hz, and *D* was determined with (A.1) with θ estimated as the mean wave direction at the ADCP sample site minus the heading separating the two instruments.

The observational time series for this calibration was 7 hours and 34 minutes in length (Figure A.2). During this time, the peak wave period was 17.6 s, which translates to 1,543 "peak" waves. The mean wave energy dissipation during this period was 0.71 W/m^2. The wave energy dissipation was assessed across 55 m, while the width of the fine-scale patch in the models is 12 m. Assuming a constant roughness of the reef flat, there are 4.5 fine-scale patches that can fit inside the 55 m separating the two instruments. Each model simulated 10 waves, with the energy dissipation estimated as the spatial and temporal mean of the volume above the bed within the fine-scale patch of the model domain. The mean energy dissipation for the level 3, 4, and 5 models were respectively 5.5 x 10^{-4}, 0.9 x 10^{-4}, and 1.6 x 10^{-3} W/m^2. Multiplying these values by 4.5 patch-widths and 154.3 per ten waves yields mean energy dissipation values of 0.38, 0.62, and 1.11 W/m^2. Based on this exercise, the level 4 model most closely matched the observed wave energy dissipation and hence was chosen as the scale for the scenario models (Section 3.6.3).

Declaration of interests

☒ The authors declare that they have no known competing financial interests or personal relationships that could have appeared to influence the work reported in this paper.

☐The authors declare the following financial interests/personal relationships which may be considered as potential competing interests:

Declarations of interest: none